A combined phase-field and cohesive zone model approach for crack propagation in layered structures made of nonlinear rubber-like materials

M.R. Marulli[a,*], A. Valverde-González[a,b], A. Quintanas-Corominas[c], M. Paggi[a], J. Reinoso[b]

[a] *IMT School for Advanced Studies Lucca, Piazza San Francesco 19, 55100 Lucca, Italy*
[b] *Grupo de Elasticidad y Resistencia de Materiales, Escuela Técnica Superior de Ingeniería, Universidad de Sevilla, Camino de los Descubrimientos s/n, 41092 Sevilla, Spain*
[c] *Barcelona Supercomputing Center (BSC), Carrer de Jordi Girona, 29, 31, 08034 Barcelona*

Abstract

The development of new high-tech products often requires the optimization of structural components having layer-based arrangements. The primary focus of the present study is the analysis of the failure mechanisms that may occur in thin layer-flexible substrate systems: crack propagation through the layers, delamination at interfaces, and Mixed-Mode mechanisms. The phase-field (PF) approach, formulated for hyperelastic materials, has been exploited through a series of tests to prove its capabilities in assessing the mechanical performance and the crack propagation mechanism of these composite structures. While the PF approach already captures the competition between crack propagation and delamination at the interface for bilayer composites having properties mismatch, as in the case of metallic or ceramic layers on rubber-like substrates, the framework has been further enriched with a Cohesive Zone Model (CZM) approach to model imperfect interfaces. The benefit of the coupled method can be noticed, especially for Mixed-Mode failure patterns, where this combination successfully captured their complexity.

Keywords: Phase-field method, Cohesive Zone Model, thin layer-substrate systems, hyperelastic materials, delamination vs. crack propagation in the bulk

1. Introduction

Nowadays, many cutting-edge technologies integrate materials with a notable mismatch between the mechanical and fracture properties of the components. This is the case of new-generation of flexible-electronic devices, bio-medical sensors, adhesive-bonded joints, and solar-cell wafers, where polymeric substrates are usually combined with stiffer layers. In the particular case of flexible electronic devices, these systems generally combine thin metallic layers (or islands) having linear elastic behavior and polymeric substrates that ensure the large deformability and flexibility of the final product.

These structural components mentioned above usually experience different failure mechanisms: (i) crack penetration into the layers from the tensile side, (ii) cohesive delamination at the interfaces between materials, and (iii) mixed-mode mechanisms integrating (i) and (ii). In this regard, previous investigations have reported the response of thin metal layers on elastomeric substrates of different Young's Modulus [1, 2], where it is possible to observe the formation of subsequent cracks in the metal layer. In line with this research, fracture and debonding of stiff ceramic islands on deformable substrates have been experimentally investigated considering different dimensions and layer thicknesses in [3].

According to the previous arguments, it can be clearly identified that the development of new high-tech products complying with layer-based arrangements requires a profound understanding of the potential failure modes and the prospective routes for possible mitigation. Within this context, the advent of numerical

*Corresponding author
Email address: mariarosaria.marulli@imtlucca.it (M.R. Marulli)

methods has been a matter of intensive research in the last three decades, where fracture modeling is still a relevant challenge in Computational Mechanics. Stemming from this need, different techniques have been proposed so far in the related literature such as the Linear Elastic Fracture Mechanics (LEFM) [4–7], the eXtended FEM (XFEM) [8–10], the numerical manifold method (NMM) [11–17], the Continuum Damage method [18–23], the Cohesive Zone Model (CZM) and the phase-field approach (PF) among many others.

Another innovative technique is the numerical manifold method (NMM), which is based on the partition of the solid regions and has been used to solve continuous and discontinuous problems adopting two levels of cover systems: the physical cover, which includes the problem domain, the boundaries and the internal discontinuities (e.g., cracks, interfaces, etc.); and the mathematical cover, which is a set of small independent domains that, even though may overlap, completely comprise the physical problem [11, 12]. This method allows discontinuities treatment without the need to conform the mesh to the solid, as long as it covers the domain. Therefore, compared to XFEM, the fracturing process can be modeled without remeshing. Concerning the applications for this novel approach, the NMM has been successfully exploited for dynamic fracture [13], hydro-mechanical systems [14] and other geotechnical engineering problems [15–17].

The CZMs are particularly efficient for pre-existing interfaces. At the same time, for modeling crack evolution within the bulk, this technique incorporates a higher level of complexity due to the need for new cohesive elements once the failure criterion is met based on re-meshing techniques. One of the main characteristics of CZMs is that the interface is allowed to experience separation in accordance with a prescribed nonlinear traction-separation law (TSL) [24–26]. Therefore, the so-called cohesive tractions increase from zero to a failure point, reaching a maximum before decreasing to zero. A review of the different interface constitutive laws can be found in [27]. This procedure has been widely applied to study crack propagation in heterogeneous materials [28, 29] or along complex interfaces [30], to model delamination of composite materials [31, 32], to simulate the adhesive layer between two components as in [33–36], as well as for applications in biological cell interactions [37].

In order to simulate crack events into continuum bodies encompassing initiation, branching, and coalescence for multiple fronts, multi-field variational formulations (usually denominated phase-field, PF, methods) have been proposed in the last decade with a tremendous impact within the research community. These techniques can be envisaged as a form of the Continuum Damage approaches, which use a parameter to describe the solid deterioration and to control the material engineering-strength [38]. PF methods are based on Griffith's vision comprising the postulation of a functional that accounts for the competition between the elastic and fracture energy counterparts. According to this theory for brittle elastic solids [39], when a crack propagates, there is a reduction of the elastic strain energy stored in the body, and, at the same time, the surface energy increases because of the creation of a new crack front. Hence a pre-existing crack will propagate if the crack growth reduces the potential energy more than the increase of surface energy. The energy released per unit of new crack surface is referred to as G. The critical value for which the crack propagates, i.e., the bulk fracture toughness, noted with G_c^b in the sequel, is a material property independent of the geometry of the solid.

Pioneering works on PF methods have been carried out by Francfort and Marigo [40], and Bourdin et al. [41]; its variational theorem has been formulated by Bourdin et al. [42] and a more engineering-based interpretation has been developed by Miehe et al. [43]. These authors consider a damage variable at the material point level as an additional primary unknown of the problem, defining an extra degree of freedom per node in the corresponding FE discretization to model brittle fracture. Further developments of PF methods were conducted for capturing cohesive [44–46], quasi-static [47, 48] and ductile [49–51] fracture events, and to dynamic crack propagation [52–54], among many others. A broader presentation of phase-field approaches can be found in [55], while extensions for modeling fatigue [56] and multi-physics coupled formulations [57] have also attracted a great deal of research in the last few years. The phase-field approach has been recently developed also in the framework of the Virtual Element Method (VEM), which represents a generalization of the standard finite element method [58, 59]. Moreover, the recent contribution [60] coupled the PF approach with the NMM in a series of standard benchmark tests for linear elastic materials.

It is worth highlighting the relevant approach carried out by Wu and Nguyen [61], which manages to propose a phase-field regularized CZM that proves to be insensitive to the length scale parameter. This innovative procedure has been exploited to analyze dynamic fracture [62], hydrogen embrittlement [63],

size effects in concrete beams [64] and many more fields of applications; and his iteration scheme has been improved to perform without requiring a high computational cost [65]. Differing from this work, Wu and Nguyen have simulated cohesive fracture in the bulk by establishing an analogy with Barenblatt's CZM [24]. Instead, in the present paper, the authors aim to simulate the coupling between the standard PF approach for brittle fracture of the bulk with cohesive interfaces to simulate the competition between crack propagation and delamination. The coupled PF-CZM approach presented here could be in principle formulated using the Wu and Nguyen approach for the bulk instead of the AT-2 approach for PF [41], which is employed here.

Concerning hyperelastic materials, a seminal contribution can be traced back to the formulation proposed by Miehe [66]. Mandal and coworkers [67] simulated crack nucleation and propagation in composites materials with polymeric matrix, while Russ et al. [68] conducted the simulation of cracking events in 3D-printed polymeric composites. In this direction, it is worth mentioning the phase-field model for a general nonlinear elastic material based on a novel energy decomposition proposed by Tang et al. [69], whereas further contributions tackling with crack nucleation and healing of micro-cracks in elastomers have been modeled in [70, 71]. In addition to this, it is important to highlight the work of [72] where damage and fracture of polymers are due to an energetic contribution that is related to the deformation of bonds in polymer chains.

Though the scientific activity on PF methods has been very active in the last decade, the understanding of fracture events in heterogeneous media has received much-limited attention so far, and it has been mostly limited to linear elastic materials. Composite materials with random distributions of inclusions in the matrix have been studied in [73] coupling the phase-field regularised CZM approach developed in [61] with Weibull random fields of the material properties. In contrast, in [74] complex micro-cracking phenomena have been simulated, introducing a regularization of the interfaces through an auxiliary scalar field. Within the same framework, Nguyen et al. [75] proposed a modeling technique for the simulation of fracture phenomena in layered structures that relies on the analysis of the material parameters mismatch and the influences of interface properties.

Another attempt to model bulk and interface fracture exploiting the phase-field approach can be found in [76, 77] where the interface delamination is addressed with the PF approach with a subtle variation in the formulation to estimate the displacement jumps and it requires particular care in the discretization and interpolation processes to avoid stress oscillations [78]. Hansen-Dörr and co-authors [79, 80] dealt with the existence of adhesive interfaces smearing the discrete interface over a certain length scale and pinpoint the addition of a compensation factor in order to avoid the interaction between the regularisation of the crack in the bulk with the interface.

Following a different methodology, Paggi and Reinoso [81] initially coupled the PF of approach with the CZM for modeling different failure mechanisms, with a special focus on composite materials and layered engineering structures. This coupled formulation efficiently follows crack propagation and branching in the bulk and models the interface interactions. In its original form, the numerical technique developed in [81] exploited a coupled approach by modifying a tension cut-off interface law according to the value of the phase-field of the surrounding bulk region.

Compared with the attempts mentioned above [61, 76–80], the combination of both PF and CZM proposed in [81] has demonstrated to facilitate the modeling of multi-layer structures due to its versatility to be adapted to a boundless number of interface laws and geometries without the necessity of modifying the configuration of the bulk model and the introduction of a diffusive interface. A proof of the potentiality of the approach is represented by its extension to brittle fracture of layered ceramics [82], poly-crystalline materials [83], solid shells [84], and microscopic failure in long fiber-reinforced composites [85] with the use of a bilinear TSL for triggering decohesion events. Moreover, a macroscopic approach for the delamination induced by matrix cracking in cross-ply laminates has been analyzed in [86].

Compared to previous works, see [81, 82, 84, 87] for the current state-of-art for this technique, the coupled PF-CZM approach has been extended to model hyperelastic materials and hence, applied to mechanical systems composed of thin layers on rubber-like substrates, which are common in many engineering applications. In general, applying the phase-field method to elastomeric materials at large deformation is more challenging than the linear elastic brittle fracture at infinitesimal strain because both material and geometric

nonlinearities should be considered simultaneously. Moreover, the material nonlinearity is also influenced by the evolution of the damage field. In order to outcome this issue, the PF approach is an effective tool to understand how the failure of a bilayer structure is affected by the properties of each component, therefore it aims to provide a characterization of the different damage patterns according to these properties, being in line with [88].

From a material perspective of the substrate, the point of departure is the constitutive model proposed in [66] including PF capabilities of fracture. Moreover, the current PF-CZM approach allows the analysis of the interaction between fractures in the bulk and the interface in the case of layered heterogeneous composites, taking into consideration also the properties of the interface, for example, in the case of an adhesive joint, and can permit the optimized designs of such structures for high-tech applications. Hence, in order to capture different failure modes, the PF technique for bulk failure in hyperelastic materials is combined with cohesive interface elements implemented considering the polynomial-based Tvergaard TSL [89, 90], which provides a gradual degradation with a larger extent of the so-called cohesive process zone (CPZ) in comparison with the cut-off TSL.

The reminder of the paper is organized as follows. Sec. 2 introduces the variational formulation of the overall system, describing the phase-field approach for finite deformation and the interface contribution. In Sec. 3 the finite element discretization of the bulk and the interface is presented. Numerical simulations exploiting the phase-field approach alone and coupled with the CZM are presented in Sec. 4.

2. Theoretical formulation

This section outlines the proposed computational framework for modeling crack propagation in layered structures. Sec. 2.1 describes the variational form of the internal energy functional of a general cracked body with the presence of prescribed interfaces. The bulk phase-field variational formulation is introduced in Sec. 2.2, whilst the interface contribution is delineated in Sec. 2.3.

2.1. Variational formulation of the system

Consider a solid in the reference configuration which domain is denoted by $\Omega_0 \subset \mathbb{R}^3$. The material points within the solid are identified by the position vector $\mathbf{X} \in \mathbb{R}^3$ with respect to the reference system. This initial configuration is considered undeformed and stress-free. Moreover, we assumed the existence of internal prescribed interfaces $\Gamma_0^i \subset \mathbb{R}^2$ in the system, and a discrete cracks network $\Gamma_0^b \subset \mathbb{R}^2$ in the bulk, see Fig. 1. They are signified together as Γ_0.

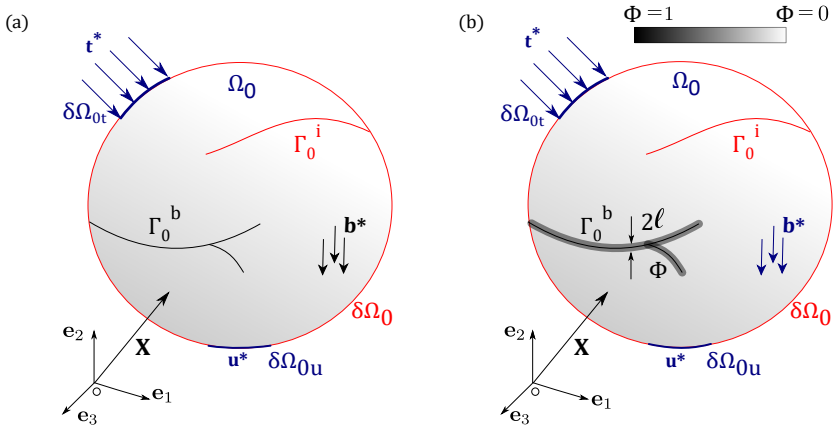

Fig. 1: A cracking solid Ω_0 in the reference configuration with an interface Γ_0^i and a sharp crack Γ_0^b in (a) and its regularization in (b).

Throughout the deformation process, the solid assumes the so-called current configuration occupying the domain denoted by $\Omega \subset \mathbb{R}^3$ at an arbitrary time t, and whose position vectors are identified by the vector $\mathbf{x}(\mathbf{X}, t)$.

Furthermore, it is possible to introduce the displacement vector which describes the motion of the body from the undeformed to the deformed configuration at the time t:

$$\mathbf{u}(\mathbf{X}, t) := \mathbf{x}(\mathbf{X}, t) - \mathbf{X} \tag{1}$$

In the quasi-static framework, the time represents only a "pseudo-time" necessary to characterize the state of deformation. Moreover, in what follows, the body's motion has been described using the total Lagrangian description, where the variables and the system equations are formulated with respect to the reference configuration and to the vector $\mathbf{X}$.

For convenience, we define the displacement jump at the interface as the relative displacement between two homologous points, i.e., $\mathbf{u} = \mathbf{u}_1 + \mathbf{u}_2$ where the interface flanks are identified by $\Gamma_0^{i,1}$ and $\Gamma_0^{i,2}$.

The deformation of the body can be characterized by the deformation gradient tensor, $\mathbf{F}$, defined as:

$$\mathbf{F} := \nabla_{\mathbf{X}}(\boldsymbol{\varphi}) = \frac{\partial \boldsymbol{\varphi}}{\partial \mathbf{X}} = \frac{\partial \mathbf{x}}{\partial \mathbf{X}} \tag{2}$$

where $\nabla_{\mathbf{X}}(\cdot)$ is the gradient of $(\cdot)$ with respect to the material configuration. The stress measure used in the present work is the first Piola-Kirchhoff tensor, $\mathbf{P}$, which can be seen as the internal force per unit deformed area.

It is also assumed that the arbitrary solid is subjected to specific body forces $\mathbf{b}^*$, while prescribed displacements $\mathbf{u}^*$ and surface tractions $\mathbf{t}^*$ are applied to some portions of the delimiting external boundary $\partial\Omega_{0,u}$ and $\partial\Omega_{0,t}$ respectively, such that $\partial\Omega_0 = \partial\Omega_{0,u} \cup \partial\Omega_{0,t}$ and $\partial\Omega_{0,u} \cap \partial\Omega_{0,t} = \emptyset$.

The external potential energy is:

$$\mathcal{P} = \int_{\Omega_0 \setminus \Gamma_0} \mathbf{b}^* \cdot \mathbf{u} \mathrm{dV} + \int_{\partial\Omega_{0,t}} \mathbf{t}^* \cdot \mathbf{u} \mathrm{dA} \tag{3}$$

The energy functional of the systems (i.e. accounting the bulk and the prescribed interfaces) reads

$$\Pi(\mathbf{u}, \Gamma_0) = \int_{\Omega_0 \setminus \Gamma_0} \psi(\mathbf{F}) \, \mathrm{dV} + \int_{\Gamma_0} G_c \, \mathrm{dA} \tag{4}$$

where the integral $\int_{\Gamma_0} G_c \mathrm{dA}$ identifies the energy dissipation due to fracture events at the crack set Γ_0^b and at the prescribed interface Γ_0^i. This contribution can be split as:

$$\Pi(\mathbf{u}, \Gamma_0) = \underbrace{\int_{\Omega_0 \setminus \Gamma_0} \psi(\mathbf{F}) \, \mathrm{dV} + \int_{\Gamma_0^b} G_c^b \, \mathrm{dA}}_{\Pi^b(\mathbf{u}, \Gamma_0^b)} + \underbrace{\int_{\Gamma_0^i} G^i \, \mathrm{dA}}_{\Pi^i(\mathbf{u}, \Gamma_0^i)} \tag{5}$$

where $\psi(\mathbf{F})$ is the Helmholtz free-energy function; G_c^b, the critical energy release rate or fracture toughness of the bulk material; and G^i, the fracture energy dissipated at the existing interface.

The total energy functional of the system can be expressed as then sum of three contributions:

$$\Pi(\mathbf{u}, \Gamma_0) = \Pi^b(\mathbf{u}, \Gamma_0^b) + \Pi^i(\mathbf{u}, \Gamma_0^i) + \mathcal{P}(\mathbf{u}) \tag{6}$$

where the bulk and the interface contributions, Π^b and Π^i respectively, have been split.

Accordingly, the variation of the total potential with respect to the primary fields, i.e. the displacement and phase-field, renders:

$$\delta\Pi(\mathbf{u}, \phi) = \delta\Pi^b + \delta\Pi^i + \delta\mathcal{P} = 0 \tag{7}$$

2.2. Phase-field variational formulation for finite deformation

The bulk contribution to the energy dissipation due to fracture can be treated considering the variational approach introduced by Francfort and Marigo [40], which evaluates the crack evolution by the substitution of the sharp crack with a transition region from undamaged to broken material. The sharp crack is approximated as a band of finite thickness characterized by a crack phase-field parameter $\phi \in [0,1]$ such that $\phi = 0$ denotes the intact material and $\phi = 1$ represents the cracked one. The crack approximation converges to the sharp crack when the band thickness approaches zero.

The energy contribution from the crack surface, contained in equation (5), is obtained through a volumetric approximation:

$$\int_{\Gamma_0^b} G_c^b \mathrm{dA} \approx \int_{\Omega_0 \setminus \Gamma_0^i} G_c^b \gamma(\phi; \nabla\phi)\, \mathrm{dV} \tag{8}$$

Accordingly the bulk strain energy functional is given by

$$\Pi^b(\mathbf{u}; \phi) = \int_{\Omega_0 \setminus \Gamma_0^i} g(\phi)\psi(\mathbf{F})\, \mathrm{dV} + \int_{\Omega_0 \setminus \Gamma_0^i} G_c^b \gamma(\phi; \nabla\phi)\, \mathrm{dV} \tag{9}$$

where $g(\phi)$ is called energetic degradation function and acts to reduce the elastic strength of the material.

There are different choices for the function $g(\phi)$, in this work we used the model introduced by Bourdin et al. in [41], usually referred to as AT2 model:

$$g(\phi) = (1-\phi)^2 + k_{\mathrm{res}} \tag{10}$$

where, in order to avoid numerical instabilities at the fully broken state, a small positive parameter k_{res} is used.

In Eq. (9), $\Gamma_0(\phi; \nabla\phi)$ is the crack surface density function that assumes this generic form:

$$\gamma(\phi, \nabla\phi) = \frac{1}{c_0}\left[\frac{1}{l_0}\alpha(\phi) + l_0 |\nabla\phi|^2\right] \tag{11}$$

where $\alpha(\phi)$ is called geometric crack function and determines the distribution of the crack phase-field, l_0 is the length scale that defines the width of the diffuse crack band, and c_0 is called scaling parameter. For the AT2 approach, the geometric crack function is $\alpha = \phi^2$ and the scaling parameter is set $c_0 = 2$.

In the related literature [91, 92], it has been shown that by assigning to l_0 a value related to the material tensile strength, σ_c^b, it is possible to predict the nucleation of fracture in the system. These authors established that the length scale is proportional to Irwin's characteristic length, $G_c^b E/(\sigma_c^b)^2$, by a factor depending on the type of phase-field model. This approach has been successfully applied to ceramics, metals, and hard polymers, showing a good agreement with experimental results [92]. Without any loss of generality, this approximation is used in the sequel, even though a detailed discussion on the use of the length scale parameter and other possible approaches can be found in [55, 67, 93], being beyond the scope of the present research. For the AT2 model, the formula reads:

$$l_0 = \frac{27}{256}\frac{G_c^b E}{(\sigma_c^b)^2} \tag{12}$$

The following variational formulation for the bulk can be derived:

$$\delta\Pi_u^b = \int_{\Omega_0 \setminus \Gamma_0^i} g(\phi)\frac{\partial\psi(\mathbf{F})}{\partial\mathbf{F}}\frac{\partial\delta\mathbf{u}}{\partial\mathbf{X}}\, \mathrm{dV} \tag{13a}$$

$$\delta\Pi_\phi^b = \int_{\Omega_0 \setminus \Gamma_0^i} \frac{\mathrm{d}g(\phi)}{\mathrm{d}\phi}\psi(\mathbf{F})\delta\phi\, \mathrm{dV} + \int_{\Omega_0 \setminus \Gamma_0^i} \frac{G_c^b}{c_0 l_0}\frac{\mathrm{d}\alpha(\phi)}{\mathrm{d}\phi}\delta\phi\, \mathrm{dV} + \int_{\Omega_0 \setminus \Gamma_0^i} \frac{2G_c^b l_0}{c_0}\Delta\phi\delta\phi\, \mathrm{dV} \tag{13b}$$

where $\delta\mathbf{u}$ and $\delta\phi$ stand for the virtual variation of the displacements and the phase-field.

The given formulation can be specified for different material models substituting the desired expression for $\psi(\mathbf{F})$. As stated before, the numerical simulations will be conducted using the expression of the strain energy potential for hyperelastic materials. Then, introducing the first Piola-Kirchhoff stress tensor $\mathbf{P} = \partial\psi(\mathbf{F})/\partial\mathbf{F}$, the formulation can be written as:

$$\delta\Pi_u^b = \int_{\Omega_0\setminus\Gamma_0^i} g(\phi)\mathbf{P}\frac{\partial\delta\mathbf{u}}{\partial\mathbf{X}}\,\mathrm{dV} \tag{14a}$$

$$\delta\Pi_\phi^b = \int_{\Omega_0\setminus\Gamma_0^i} \frac{\mathrm{d}g(\phi)}{\mathrm{d}\phi}\psi(\mathbf{F})\delta\phi\,\mathrm{dV} + \int_{\Omega_0\setminus\Gamma_0^i} \frac{G_c^b}{c_0 l_0}\frac{\mathrm{d}\alpha(\phi)}{\mathrm{d}\phi}\delta\phi\,\mathrm{dV} + \int_{\Omega_0\setminus\Gamma_0^i} \frac{2G_c^b l_0}{c_0}\Delta\phi\delta\phi\,\mathrm{dV} \tag{14b}$$

According to [66], the strain energy function is written in terms of right Cauchy-Green tensor $\mathbf{C} = \mathbf{F}^{\mathrm{T}}\mathbf{F}$ as:

$$\psi(\mathbf{C}) = \frac{\mu}{2}\left[\mathrm{tr}(\mathbf{C}) - 3\right] + \frac{\mu}{\beta}\left[J^{-\beta} - 1\right] \tag{15}$$

where $J = det(\mathbf{F})$, μ is the shear modulus and $\beta = 2\nu/(1-2\nu) > 0$ describes a weak volumetric compressibility of the elastic solid through the Poisson ratio ν.

The first Piola-Kirchhoff stress tensor is given by:

$$\mathbf{P} = \mu\left[\mathbf{F} - J^{-\beta}\mathbf{F}^{-\mathrm{T}}\right] \tag{16}$$

The linearization of the weak form equations of the system introduced later in Sec. 3 requires the computation of the first elasticity tensor $\mathbb{A}^{(1)}$ [94]. This operator is used in the Newton-Raphson solution method in fully implicit nonlinear FE schemes. The first elasticity tensor in component notation can be computed starting from Eq. (16) as:

$$\mathbb{A}^{(1)}_{iIjJ} = \frac{\partial^2\psi}{\partial F_{Ii}\partial F_{Jj}} = \left[\mu\delta_{ij}\delta_{IJ} + \mu\beta J^{-\beta}F^{-1}_{Ii}F^{-1}_{Jj} + \mu J^{-\beta}F^{-1}_{iI}F^{-1}_{jJ}\right] \tag{17}$$

2.3. Variational formulation of the interface contribution

The formulation is here described in a 2D setting for the sake of simplicity in the derivation, however, the generalization in 3D is straightforward, see [95]. For the description of the interface contribution to the energy functional of the solid, it is necessary to introduce the displacement jump, $\Delta\mathbf{u}$, given by the relative displacement $\mathbf{g} = \mathbf{u}_1 - \mathbf{u}_2$ between the two sides of the interface Γ_0^i. The displacement jump can also be described as the gap field across the interface $\mathbf{g} = (g_{\mathrm{n}}, g_{\mathrm{t}})^{\mathrm{T}}$, in the local reference defined by the normal and tangential unit vectors, $\mathbf{n}$ and $\mathbf{t}$, at the interface.

The interface energy dissipation due to crack opening phenomena can be written as function of the gap field and in terms of the Piola-Kirchhoff cohesive traction $\mathbf{T} = (\tau, \sigma)^{\mathrm{T}}$ as:

$$\Pi^i(\mathbf{g}, \Gamma_0^i) = \int_{\Gamma_0^i} G^i(\mathbf{g})\mathrm{dA} = \int_{\Gamma_0^i} \mathbf{g}^{\mathrm{T}}\mathbf{T}\mathrm{dA} \tag{18}$$

The variation of the previous expression reads

$$\delta\Pi^i = \delta\mathbf{u}^{\mathrm{T}}\int_{\Gamma_0^i}\left(\frac{\partial\mathbf{g}}{\partial\mathbf{u}}\right)^{\mathrm{T}}\mathbf{T}\mathrm{dA} \tag{19}$$

The constitutive relation of an interface has been modeled in this paper by the TSL proposed by Tvergaard [89] with the addition of a nonlinear unloading relationship described by Espinosa and Zavattieri [90]. This interface model describes the dependence of the cohesive traction on displacement jumps through a polynomial law.

Since both the normal and the tangential behaviors should be considered, a non-dimensional effective displacement λ is introduced:

$$\lambda = \sqrt{\left(\frac{g_n}{g_{\mathrm{nc}}}\right)^2 + \left(\frac{g_t}{g_{\mathrm{tc}}}\right)^2} \tag{20}$$

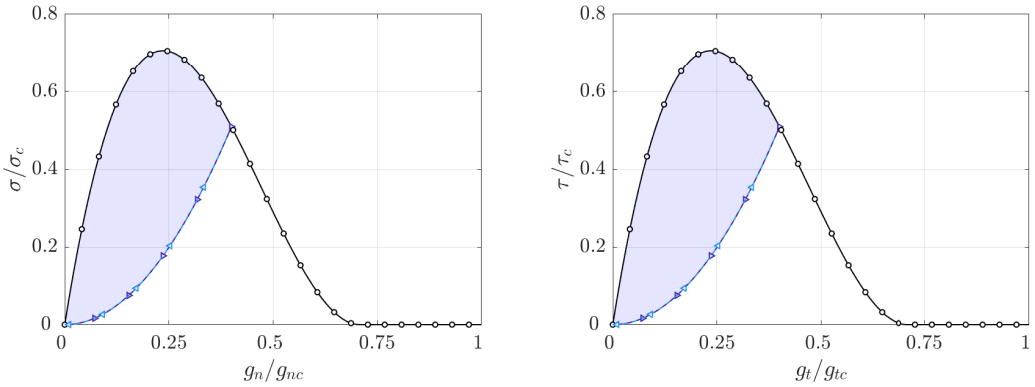

Fig. 2: Tvergaard cohesive law with unloading and reloading at $\lambda = 0.4$.

where g_{nc} and g_{tc} are the critical gap values corresponding to the interface failure.

The tangential and normal cohesive tractions τ and σ in case of monotonic loading are computed as:

$$\sigma = \frac{g_n}{g_{\mathrm{nc}}}\sigma_{\mathrm{c}} P(\lambda) \tag{21a}$$

$$\tau = \frac{g_t}{g_{\mathrm{tc}}}\tau_{\mathrm{c}} P(\lambda) \tag{21b}$$

where the polynomial factor $P(\lambda)$ is defined by:

$$P(\lambda) = \frac{27}{4}(1 - 2\lambda + \lambda^2) \tag{22}$$

Moreover, in case of an unloading of the interface, the traction relations depends on the value assumed by λ at the last step before unloading, here referred as λ_{u}. Hence, the unloading and reloading are governed by the following expressions under a nonlinear behavior:

$$\sigma = \frac{g_n}{g_{\mathrm{nc}}}\sigma_{\mathrm{c}} P(\lambda_{\mathrm{u}})\frac{\lambda}{\lambda_u} \qquad \text{if } \lambda < \lambda_u \tag{23a}$$

$$\tau = \frac{g_t}{g_{\mathrm{tc}}}\tau_{\mathrm{c}} P(\lambda_{\mathrm{u}})\frac{\lambda}{\lambda_u} \qquad \text{if } \lambda < \lambda_u \tag{23b}$$

The described interface constitutive law is depicted in Fig. 2 for the tangential and the normal directions.

In order to elucidate the physical state of the interface, a damage variable $\mathcal{D}$ is introduced in the interval $\lambda_{\mathrm{cr}} < \lambda < 1$ where $\lambda_{\mathrm{cr}} = 1/3$ represents the value of the effective gap at which the tractions are maximum. Hence the interface is considered to be intact until λ_{cr}, and the following boundaries are given for the damage variable:

$$\mathcal{D} = \begin{cases} 0 & \text{if } \lambda < \lambda_{cr} \\ 2\lambda^2 - \lambda^4 & \text{if } \lambda_{cr} \leq \lambda < 1 \\ 1 & \text{if } \lambda = 1 \end{cases} \tag{24}$$

Moreover in case of unloading, the damage is obtained considering the maximum effective gap reached λ_u: $\mathcal{D} = 2\lambda_u^2 - \lambda_u^4$.

The expression of the damage variable derives from energetic considerations as already proposed in [90]. Considering pure mode I or mode II, the expressions for the energy release rate G_{I} and G_{II} are obtained through the integration of the traction-separation law expressed in Eqs. (21a)-(21b):

$$G_{\mathrm{I}} = \frac{9}{16}\sigma_{\mathrm{c}} g_n (6\lambda - 8\lambda^2 + 3\lambda^3) \qquad G_{\mathrm{II}} = \frac{9}{16}\tau_{\mathrm{c}} g_t (6\lambda - 8\lambda^2 + 3\lambda^3) \tag{25}$$

Considering the fully broken state, i.e. $\lambda = 1$, $g_n = g_{nc}$ and $g_t = g_{tc}$; the critical strain energy release rate G_{IC} and G_{IIC}, which represent the area under the traction-displacement curves, are given by:

$$G_{\mathrm{IC}} = \frac{9}{16}\sigma_{\mathrm{c}} g_{\mathrm{nc}} \qquad G_{\mathrm{IIC}} = \frac{9}{16}\tau_{\mathrm{c}} g_{\mathrm{tc}} \tag{26}$$

In case of unloading at λ_u, the dissipated energy is given by the blue area highlighted in Fig. 2 which can be computed through Eqs. (21a)-(21b) and Eqs. (23a)-(23b) as:

$$G^{\mathrm{d}}_{\mathrm{IC}} = \frac{9}{16}\sigma_{\mathrm{c}} g_{\mathrm{nc}} (6\lambda_{\mathrm{u}}^2 - 8\lambda_{\mathrm{u}}^3 + 3\lambda_{\mathrm{u}}^4) - \frac{27}{48}\sigma_{\mathrm{c}} g_{\mathrm{nc}} (4\lambda_{\mathrm{u}}^2 - 8\lambda_{\mathrm{u}}^3 + 4\lambda_{\mathrm{u}}^4) = \frac{9}{16}\sigma_{\mathrm{c}} g_{\mathrm{nc}} (2\lambda_u^2 - \lambda_u^4) \tag{27a}$$

$$G^{\mathrm{d}}_{\mathrm{IC}} = \frac{9}{16}\tau_{\mathrm{c}} g_{\mathrm{tc}} (6\lambda_{\mathrm{u}}^2 - 8\lambda_{\mathrm{u}}^3 + 3\lambda_{\mathrm{u}}^4) - \frac{27}{48}\tau_{\mathrm{c}} g_{\mathrm{tc}} (4\lambda_{\mathrm{u}}^2 - 8\lambda_{\mathrm{u}}^3 + 4\lambda_{\mathrm{u}}^4) = \frac{9}{16}\tau_{\mathrm{c}} g_{\mathrm{tc}} (2\lambda_u^2 - \lambda_u^4) \tag{27b}$$

The ratio of the energy dissipated in case of unloading of the interface with respect to the critical energy release rate can be written as:

$$\frac{G^{\mathrm{d}}_{\mathrm{IC}}}{G_{\mathrm{IC}}} = \frac{G^{\mathrm{d}}_{\mathrm{IC}}}{G_{\mathrm{IIC}}} = 2\lambda_u^2 - \lambda_u^4 \tag{28}$$

Hence, this leads to the expression of the damage variable that is indicated at Eq. (24).

From a numerical perspective, the nonlinear Newton-Raphson solution scheme requires the computation of the tangent operator $\mathbb{C} = \partial \mathbf{T}/\partial \mathbf{g}$. The expressions for each component are analytically derived from the above-given equations for the tractions, having this matrix the form of

$$\mathbb{C} = \begin{bmatrix} \dfrac{\partial \tau}{\partial g_t} & \dfrac{\partial \tau}{\partial g_n} \\ \dfrac{\partial \sigma}{\partial g_t} & \dfrac{\partial \sigma}{\partial g_n} \end{bmatrix} \tag{29}$$

Notice that in the case of a compression state of the interface along the normal direction, a penalty parameter k_{pe} is used to avoid penetration. Hence, the complete interface law in the normal direction reads:

$$\sigma = \begin{cases} \dfrac{g_n}{g_{\mathrm{nc}}}\sigma_c P(\lambda) & \text{if } g_n \geq 0 \text{ and } \lambda \geq \lambda_u \\ \dfrac{g_n}{g_{\mathrm{nc}}}\sigma_c P(\lambda_u) & \text{if } g_n \geq 0 \text{ and } \lambda < \lambda_u \\ k_{\mathrm{pe}} g_n & \text{if } g_n < 0 \end{cases} \tag{30}$$

where the penalty parameter $k_{\mathrm{pe}} = 10^3$ is assumed in the numerical simulations unless otherwise noted.

For the tangential direction, the interface law is written as:

$$\tau = \begin{cases} \dfrac{g_t}{g_{\mathrm{tc}}}\tau_c P(\lambda) & \text{if } \lambda \geq \lambda_u \\ \dfrac{g_t}{g_{\mathrm{tc}}}\tau_c P(\lambda_u) & \text{if } \lambda < \lambda_u \end{cases} \tag{31}$$

3. Finite element formulation of the system

This section presents the finite element formulation for the bulk and the interface. They are introduced in Sec. 3.1 and in Sec. 3.2 respectively.

3.1. Finite element discretization of the bulk

The displacement field $\mathbf{u}$ is interpolated in terms of nodal displacements $\bar{\mathbf{u}}$ as:

$$\mathbf{u}(\mathbf{X}) \approx \sum_a \mathbf{N}_a(\boldsymbol{\xi}_a)\bar{\mathbf{u}}_a = \mathbf{N}(\boldsymbol{\xi})\bar{\mathbf{u}} \tag{32}$$

where $\boldsymbol{\xi} = \{\xi_1, \xi_2\}$ are the natural coordinates for each element in the two-dimensional case, $\mathbf{N}_a$ is the shape function matrix associated with node a (with the shape function N_a at the diagonal terms), and $\mathbf{N}(\boldsymbol{\xi})$ is matrix operator collecting the standard linear shape function at the element level.

The virtual displacement field is approximated using the same shape functions as:

$$\delta\mathbf{u}(\mathbf{X}) \approx \sum_a \mathbf{N}_a(\boldsymbol{\xi})\delta\bar{\mathbf{u}}_a = \mathbf{N}(\boldsymbol{\xi})\delta\bar{\mathbf{u}} \tag{33}$$

The displacement derivatives with respect to the reference system are computed as:

$$\mathbf{u}_{a,J} = \frac{\partial \mathbf{u}_a}{\partial X_J} = \sum_a N_{a,J}\bar{\mathbf{u}}_a \tag{34}$$

where the notation $\square_{,J}$ is used to express the derivative of a variable $\square$ with respect to X_J.

In order to express the weak form equations, the columns of matrix $\mathbf{B}$ containing the derivatives of the shape functions can be expressed, for a 2D setting, as:

$$\mathbf{B}_a = \begin{bmatrix} N_{a,1} \\ N_{a,2} \end{bmatrix} \tag{35}$$

Similarly, for the phase-field ϕ and its gradient $\nabla\phi$ the interpolation in terms of nodal values $\bar{\boldsymbol{\phi}}$ reads:

$$\phi \approx \sum_a \bar{N}_a(\boldsymbol{\xi})\bar{\phi}_a = \bar{\mathbf{N}}\bar{\boldsymbol{\phi}} \tag{36}$$

$$\delta\phi \approx \sum_a \bar{N}_a(\boldsymbol{\xi})\delta\bar{\phi}_a = \bar{\mathbf{N}}\delta\bar{\boldsymbol{\phi}} \tag{37}$$

$$\boldsymbol{\nabla\phi} \approx \sum_a \bar{\mathbf{B}}_a(\boldsymbol{\xi})\bar{\phi}_i = \bar{\mathbf{B}}\bar{\boldsymbol{\phi}} \tag{38}$$

where $\bar{\mathbf{N}}$ is the standard interpolation operator for the phase-field and $\bar{\mathbf{B}}$ is the kinematic operator that approximates the phase-field spatial gradient. Their specific expressions can be found in [96].

With the above approximations, the weak form of the nonlinear Eq. (14) after the insertion of the previous interpolation scheme is given by:

$$\delta\Pi_u = (\delta\bar{\mathbf{u}})^{\mathbf{T}}\left(\mathbf{f}^{\text{ext}} - \int_{\Omega_0} \mathbf{B}^{\mathrm{T}} g(\phi)\mathbf{P}\mathrm{dV}\right) = 0 \tag{39a}$$

$$\delta\Pi_\phi = (\delta\bar{\boldsymbol{\phi}})^{\mathrm{T}}\int_{\Omega_0} \bar{\mathbf{N}}^{\mathrm{T}}\left(g'(\phi)\psi(\mathbf{F}) + \frac{G_c^b}{c_0 l_0}\alpha'(\phi)\right)\mathrm{dV} + (\delta\bar{\boldsymbol{\phi}})^{\mathrm{T}}\int_{\Omega_0} \frac{2G_c^b l_0}{c_0}\bar{\mathbf{B}}^{\mathrm{T}}\bar{\mathbf{B}}\bar{\boldsymbol{\phi}}\mathrm{dV} = 0 \tag{39b}$$

The internal residuals that are required for the nonlinear Newton-Raphson solution scheme of the corresponding finite element problem take the form:

$$\mathbf{r}_u^i = -\int_{\Omega_0} \mathbf{B}^{\mathrm{T}} g(\phi)\mathbf{P}\mathrm{dV} = 0 \tag{40a}$$

$$\mathbf{r}_\phi^i = \int_{\Omega_0} \left[\bar{\mathbf{N}}^{\mathrm{T}}\left(g'(\phi)\psi(\mathbf{F}) + \frac{G_c^b}{c_0 l_0}\alpha'(\phi)\right) + \frac{2G_c^b l_0}{c_0}\bar{\mathbf{B}}^{\mathrm{T}}\bar{\mathbf{B}}\bar{\boldsymbol{\phi}}\right]\mathrm{dV} = 0 \tag{40b}$$

From a numerical perspective, the current FE formulation is implemented into the implicit form of the package `ABAQUS` using the user-defined `UEL` capability. In particular, a staggered solution method is used to solve the discretized system of equations as in [96]. For this purpose, at each time step, the current displacement is computed using the phase-field value at the previous step, while the current phase-field is calculated based on the energy history. Correspondingly, the weak form of the displacement problem at the time step $n+1$ is formulated as follows:

$$\mathbf{r}_u^i = -\int_{\Omega_0} \mathbf{B}^{\mathrm{T}} g(\phi^n)\mathbf{P}\mathrm{dV} = 0 \tag{41}$$

This equation is solved for $\mathbf{u}$, assuming ϕ^n known from the previous time step.

Similarly the phase-field problem is written as:

$$\mathbf{r}_\phi^i = -\int_{\Omega_0} \left[\bar{\mathbf{N}}^{\mathrm{T}}\left(g'(\phi)\mathcal{H}^{n+1} + \frac{G_c^b}{c_0 l_0}\alpha'(\phi)\right) + \frac{2G_c^b l_0}{c_0}\bar{\mathbf{B}}^{\mathrm{T}}\bar{\mathbf{B}}\bar{\boldsymbol{\phi}}\right]\mathrm{dV} = 0 \tag{42}$$

where the potential energy from the displacement problem is replaced by a history variable defined as:

$$\mathcal{H}^0 = 0 \tag{43a}$$

$$\mathcal{H}^{n+1} = \max\{\psi(\mathbf{F}^n), H^n\} \tag{43b}$$

Finally, the consistent tangent matrix are computed by conducting the consistent linearization of the residual equations. Then, the global system of equations renders:

$$\begin{bmatrix}\mathbf{K}^{uu} & \mathbf{0}\\ \mathbf{0} & \mathbf{K}^{\phi\phi}\end{bmatrix}\begin{bmatrix}\Delta\mathbf{u}\\ \Delta\phi\end{bmatrix} = \begin{bmatrix}\mathbf{r}_u\\ \mathbf{r}_\phi\end{bmatrix} \tag{44}$$

where $\Delta\mathbf{u}$ and $\Delta\phi$ are the new nodal solutions at the time step $n+1$, and the residuals are given by $\mathbf{r}_u = \mathbf{r}_u^e - \mathbf{r}_u^i$ and $\mathbf{r}_\phi = \mathbf{r}_\phi^e - \mathbf{r}_\phi^i$, where the terms with the superscript e denote the external contribution.

The terms of the matrix $\mathbf{K}^{uu}$ can be obtained as [97]:

$$\mathbf{K}_{ab}^{uu} = \int_{\Omega_0} \frac{\partial N_a}{\partial X_I}\mathbb{A}_{IJ}\frac{\partial N_b}{\partial X_J}\mathrm{dV}, \tag{45}$$

whereas from the phase-field residual in Eq. (42), the tangent matrix $\mathbf{K}^{\phi\phi}$ is computed as:

$$\mathbf{K}^{\phi\phi} = \int_{\Omega_0} \left[\left(g''(\phi)\mathcal{H} + \frac{G_c^b}{c_0 l_0}\alpha''(\phi)\right)\bar{\mathbf{N}}^{\mathrm{T}}\bar{\mathbf{N}} + \frac{2G_c^b l_0}{c_0}\bar{\mathbf{B}}^{\mathrm{T}}\bar{\mathbf{B}}\right]\mathrm{dV} \tag{46}$$

3.2. Finite element discretization of the interface

In order to evaluate the displacement gap $\mathbf{g}$ at any point inside the interface finite element represented in Fig. 3, we need to introduce the interface nodal displacement vector $\mathbf{d} = (u_{e_1}^1, u_{e_2}^1, \ldots, u_{e_1}^4, u_{e_2}^4)^{\mathrm{T}}$, which collects the displacements $u_{e_1}^i$ and $u_{e_2}^i$ (with $i = 1, ..., 4$) of the four interface finite element nodes.

The relative displacement $\mathbf{g}$ for the nodes 1-4 and 2-3 is then computed by applying a matrix operator $\mathbf{L}$ which calculates the difference between the displacements of nodes 1 and 2 with respect to those of nodes 4 and 3. The relative displacement within the interface finite element is then given by the linear interpolation

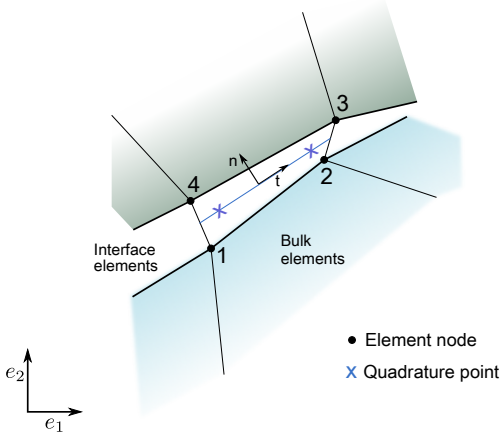

Fig. 3: Sketch of the interface finite element topology in case of a 2D setting.

of the corresponding nodal values, represented by the multiplication with the matrix $\hat{\mathbf{N}}$ which collects the shape functions at the element level.

Finally, the tangential and the normal gaps are determined by the multiplication with the rotation matrix $\mathbf{R}$ defined by the components of the unit vectors $\mathbf{t}$ and $\mathbf{n}$. This operation is due to the necessity of transforming the relative displacement computed as $\mathbf{Ld}$ in the global reference system to the local reference system of the interface finite element. In the formula, we have:

$$\mathbf{g} = -\mathbf{R}\hat{\mathbf{N}}\mathbf{L}\mathbf{d}, \tag{47}$$

where the operators' expressions are described in details in [98]. To shorten the notation, it can be introduced the interface compatibility operator $\hat{\mathbf{B}} = \hat{\mathbf{N}}\mathbf{L}$.

The term $\partial\mathbf{g}/\partial\mathbf{u}$ entering in Eq. 19 can be approximated as:

$$\frac{\partial \mathbf{g}}{\partial \mathbf{u}} \approx \frac{\partial \mathbf{g}}{\partial \mathbf{d}} = \mathbf{R}\hat{\mathbf{B}} + \frac{\partial \mathbf{R}}{\partial \mathbf{d}}\hat{\mathbf{B}}\mathbf{d} \tag{48}$$

With the introduced approximations, the interface contribution in equation (19) can be expressed as:

$$\delta\Pi^i = \delta\mathbf{d}^{\mathrm{T}} \int_{\Gamma_0^i} \left(\mathbf{R}\hat{\mathbf{B}} + \frac{\partial \mathbf{R}}{\partial \mathbf{d}}\hat{\mathbf{B}}\right)^{\mathrm{T}} \mathbf{T}\mathrm{dA} \tag{49}$$

where $\delta\mathbf{d}$ stands for the kinematically admissible virtual nodes displacements at the interface.

The solution of the variational equation requires the following residual vector:

$$\mathbf{r}_d = \int_{\Gamma_0^i} \left(\mathbf{R}\hat{\mathbf{B}} + \frac{\partial \mathbf{R}}{\partial \mathbf{d}}\hat{\mathbf{B}}\right)^{\mathrm{T}} \mathbf{T}\,\mathrm{dA} \tag{50}$$

Moreover, the element stiffness matrix, necessary for the Newton-Raphson procedure, can be obtained from the linearization of the residual. In the hypothesis of large displacements, since the rotation operator $\mathbf{R}(\mathbf{u})$ depends on the displacement field, the linearization leads to the so-called geometrical stiffness matrix. Hence the element stiffness matrix for the interface finite element, $\mathbf{K}_{dd}$, is given by the material and the geometrical

contributions:

$$\mathbf{K}_{dd} = \mathbf{K}_{dd}^{\mathrm{mat}} + \mathbf{K}_{dd}^{\mathrm{geo}} \tag{51a}$$

$$\mathbf{K}_{dd}^{\mathrm{mat}} = \int_{\Gamma_0^i} \hat{\mathbf{B}}^{\mathrm{T}} \mathbf{R}^{\mathrm{T}} \mathbb{C} \mathbf{R} \hat{\mathbf{B}} \, \mathrm{dA} \tag{51b}$$

$$\mathbf{K}_{dd}^{\mathrm{geo}} = \int_{\Gamma_0^i} \left[2\hat{\mathbf{B}}^{\mathrm{T}} \frac{\partial \mathbf{R}^{\mathrm{T}}}{\partial \mathbf{d}} \mathbf{T} + \mathbf{d}^{\mathrm{T}} \hat{\mathbf{B}}^{\mathrm{T}} \frac{\partial \mathbf{R}^{\mathrm{T}}}{\partial \mathbf{d}} \mathbb{C} \frac{\partial \mathbf{R}}{\partial \mathbf{d}} \hat{\mathbf{B}} \mathbf{d} + \left(\hat{\mathbf{B}}^{\mathrm{T}} \mathbf{R}^{\mathrm{T}} \mathbb{C} \frac{\partial \mathbf{R}}{\partial \mathbf{d}} \hat{\mathbf{B}} \mathbf{d} + \mathbf{d}^{\mathrm{T}} \hat{\mathbf{B}}^{\mathrm{T}} \frac{\partial \mathbf{R}^{\mathrm{T}}}{\partial \mathbf{d}} \mathbb{C} \mathbf{R} \hat{\mathbf{B}} \right) \right] \mathrm{dA} \tag{51c}$$

The detailed derivations of the previous contributions can be found in [98].

4. Numerical simulations

The formulation of the current phase-field hyperelastic formulation is first examined by considering plane strain, plane stress, and 3D cases through benchmark tests taken from the literature, see Appendix A. In this section, the capability of the phase-field framework for the 3D simulations is only explored in the case of a thin cylindrical structure and it will be further explored in future investigations.

After the previous verification, the proposed computational framework is employed for modelling cracking events in thin-walled structures composed of two different layers with mechanical parameters mismatch. The simulations aim to reproduce the crack propagation within structures that involve materials with significantly different Young's Modulus and fracture energy.

The first application under analysis, described in Sec. 4.1, considers a notched 2D plate with two different thin layers. Exploiting the phase-field approach for the bulk, a parametric study on the fracture propagation through the layers is conducted varying fracture toughness and bulk properties between the joint materials to understand the competition between crack branching and penetration when the crack impinges the interface represented by the materials discontinuity.

In addition to the previous parametric studies, the following two sections deal with realistic applications of the framework to stretchable electronics. An interesting application considering a thin linear elastic material layer on top of a hyperelastic one is first proposed. These simulations have been conducted using the phase-field approach without interface in Sec. 4.2.

A comparison of the crack paths obtained using the phase-field approach for the bulk in combination with CZMs for interface cracking is presented in Sec. 4.3. This application is chosen in order to show that the simulation of complex failure mechanism benefits from the introduction of the interface. The cohesive interface is equipped with the polynomial-based Tvergaard TSL between the thin elastic layer and the polymeric substrate with this aim.

The last application considers ceramic islands on top of a polyimide substrate as was tested by [3], exploiting the proposed framework to simulate different failure modes involving cracking and debonding of the structure.

4.1. Bilayered joint with parameters mismatch

The analysis proposed in this section concerns a structural joint composed of two layers with different mechanical and geometrical properties. The failure of a joint subjected to a uniform tensile condition is simulated using the proposed hyperelastic PF formulation. With the aim of understanding which parameters can affect the failure of the joint, a parametric study is conducted considering: (i) Young's Modulus ratio between the two layers, (ii) critical fracture energies mismatch, and (iii) thickness of the joined components.

The geometry of the sample is given in Fig. 4 together with the applied boundary conditions. The current simulation is conducted under plane strain assumption. Moreover, in order to keep the consistency in the analysis, the total height of the joint is constant and equal to 10 mm, while the ratio between the upper and lower layer thickness may vary. In this latter case, the notch depth varies so that it is always half of the upper layer thickness.

Both the layers are modeled using the Neo-Hookean constitutive model described in Sec. 2.2. Concerning the mechanical parameters, the lower layer is considered as made of PET (PolyEthylene Terephthalate), one

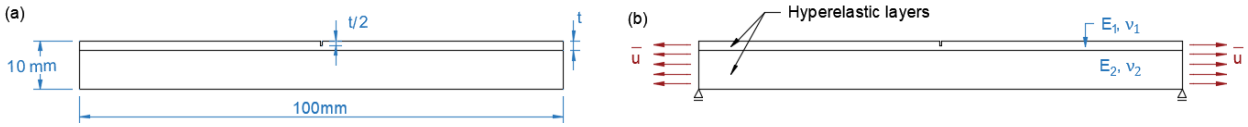

Fig. 4: Geometry (a) and boundary conditions (b) of a bilayer rectangular plate with a notch in the top layer. The simulations include thickness of $t = 1.0, 2.0\,\text{mm}$.

of the most common polymers used for packaging, in the form of containers for food and liquids, and as the substrate in solar cells and flexible electronics, and for 3D printing products. Its material properties are reported in the Tab. 1. The length scale parameter has been computed using E and $\boldsymbol{\sigma}_c$ as given in the table through Eq. (12). The same procedure has been applied for the other materials in the present work.

Material	**E** [GPa]	ν	λ [GPa]	μ [GPa]	$\mathbf{G_c}$ [N/mm]	$\boldsymbol{\sigma}_c$ MPa	$\mathbf{l_0}$ [mm]
PET	2.80	0.37	2.91	1.02	10.34	55	1.00

Tab. 1: Mechanical parameters of the polymer PET (Polyethylene terephthalate), taken from [84, 99].

The properties of the upper layer are reported in Tab. 1 as well, except for the Young's Modulus and the critical fracture energy that will take different values in order to assess the impact of the specific parameter for the current study case.

Regarding the underlying FE discretization and to avoid mesh influence on the results, a convergence study has been carried out on the element dimension, choosing the value of $h = 0.2\,\text{mm}$.

4.1.1. Young's Modulus influence

The first parameter for the joint analysis is the Young's Modulus ratio between the two layers E_1/E_2, where E_1 and E_2 refer to the upper and lower layers, respectively. The considered range accounts for different orders of magnitude from $E_1/E_2 = 0.001$ to $E_1/E_2 = 100$. The study aims to assess how different stiffness values of the upper layer can change the crack initiation and propagation. The analysis is repeated for two different upper layer thicknesses: $t = 1.0,\ 2.0\,\text{mm}$.

The imposed displacement-reaction force results are depicted in Fig. 5. It can be noticed immediately that a higher Young's Modulus ratio corresponds to a smaller prescribed displacement for the failure of the joint for both the upper layer thickness considered. For $E_1/E_2 = 100$, after a sudden drop of the reaction force caused by the propagation of the crack in the upper layer, when the crack arrives at the interface, the reaction force curve shows a second stage due to the propagation of the crack into the lower layer with a lower Young's Modulus.

The crack path for the different stiffness ratios in the undeformed configuration is shown in Figs. 6-12, comparing for each case the results for the two values of thickness of the upper layer. Analyzing these graphs, it can be observed that the thickness of the layers does not strongly influence the predicted crack path. Moreover, the first three cases (Figs. 6-8) are characterized by an upper layer more flexible than the substrate. For such cases, despite the presence of the notch, the failure phenomenon is predicted to commence from the lower layer. It can also be noticed that, before the propagation in the upper layer, the damage tends to propagate within the substrate and along the interface.

The case in Fig. 9 is reported only for comparison since, in this case, the same parameters are used for the upper and lower layer; hence the plate is composed only of one material. The crack development has been detailed in Fig. 10 for the system with upper layer thickness $t = 2\,\text{mm}$ in the deformed configuration.

The triangular shape of the crack band visible in the undeformed contour plot in Fig. 10f can be related to the deformation process related to the crack propagation, or it might be related to the appearance of the phenomenon of crazing. In order to elucidate this, an extension of the framework to dynamic fracture would be required, and it could be an interesting future development. In such a field, a recent contribution by [100] deals with layered composites employing a phase-field approach with CZM interfaces in dynamics, and the investigation could be extended to finite strain and hyperelastic materials.

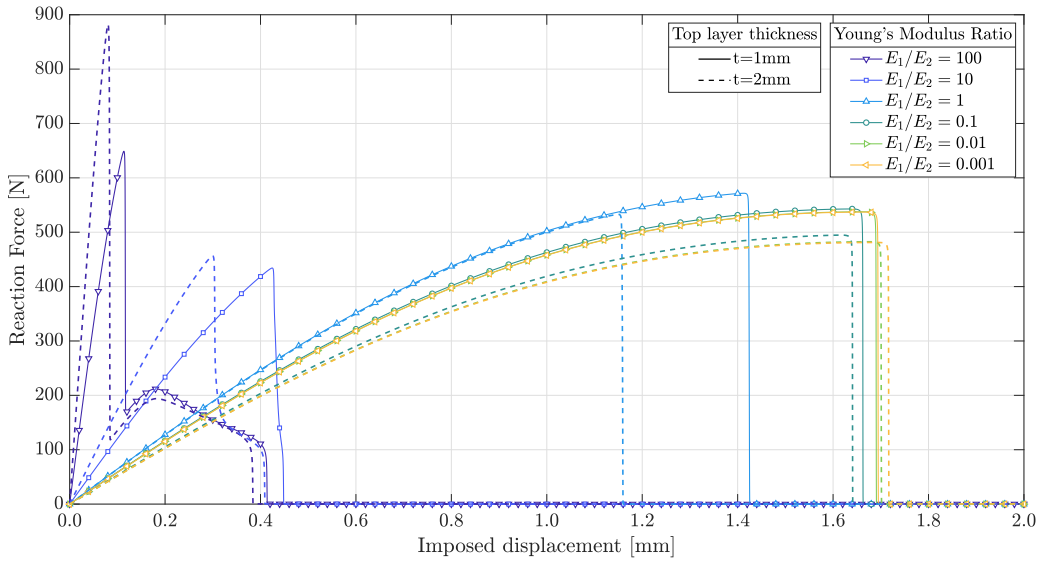

Fig. 5: Parametric study on the effect of Young's Modulus mismatch in a bilayer structure. For the lower layer, the PET material parameters have been used (see Tab. 1), varying the top layer thickness and its value of Young's Modulus E_1.

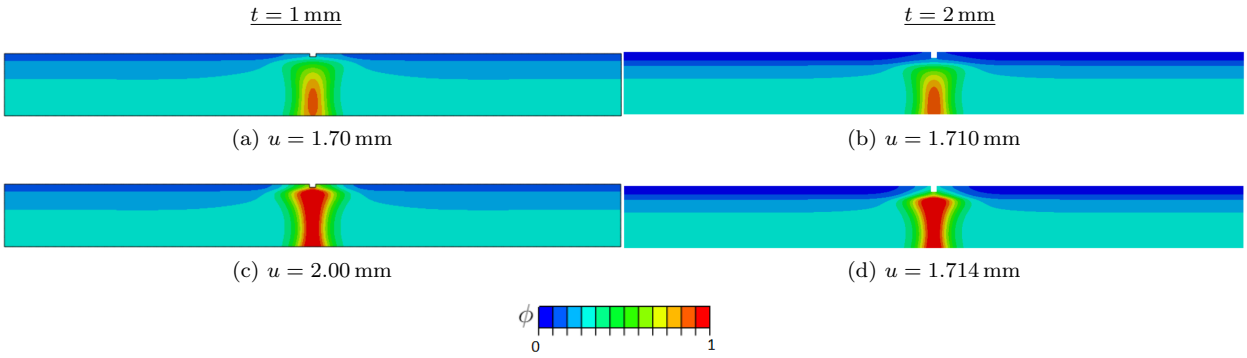

(a) $u = 1.70\,\text{mm}$ (b) $u = 1.710\,\text{mm}$

(c) $u = 2.00\,\text{mm}$ (d) $u = 1.714\,\text{mm}$

Fig. 6: Crack evolution for Young's Modulus ratio $E_1/E_2 = 0.001$.

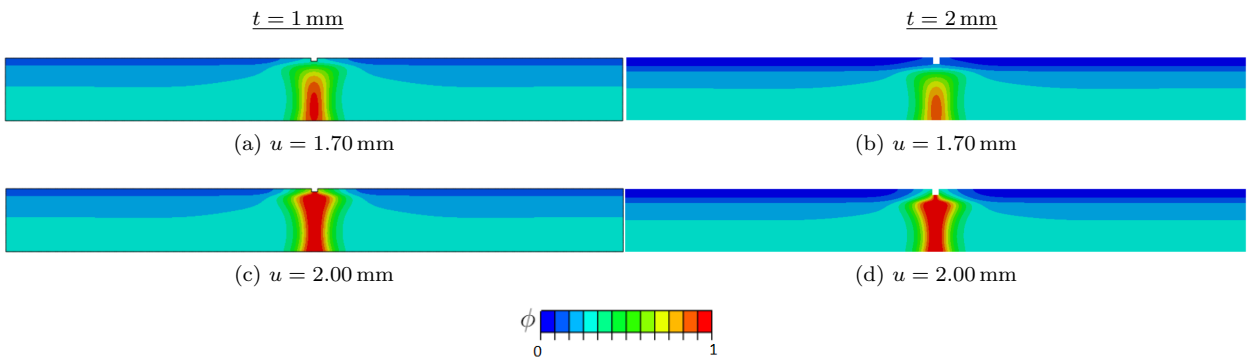

(a) $u = 1.70\,\text{mm}$ (b) $u = 1.70\,\text{mm}$

(c) $u = 2.00\,\text{mm}$ (d) $u = 2.00\,\text{mm}$

Fig. 7: Crack evolution for Young's Modulus ratio $E_1/E_2 = 0.01$.

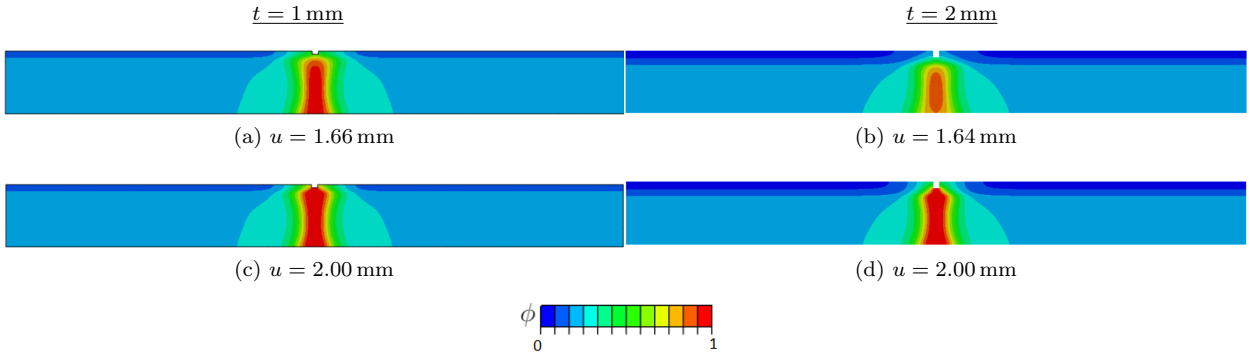

Fig. 8: Crack evolution for Young's Modulus ratio $E_1/E_2 = 0.1$.

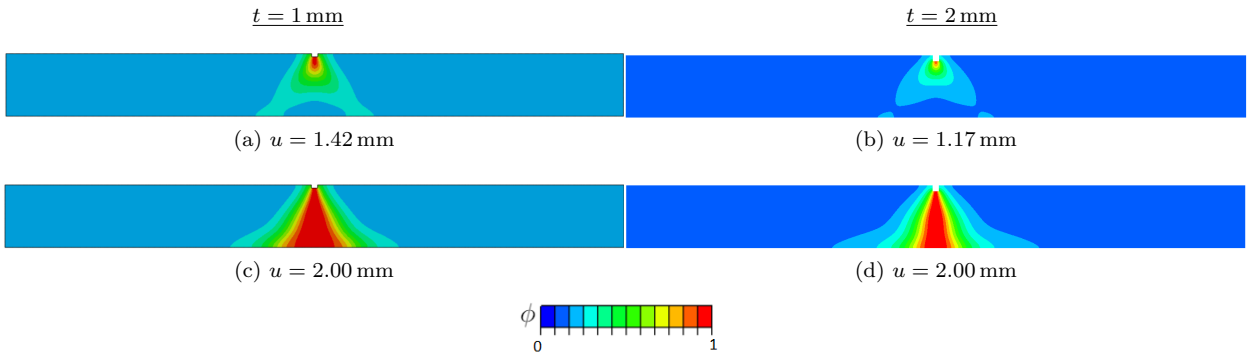

Fig. 9: Crack evolution for Young's Modulus ratio $E_1/E_2 = 1$.

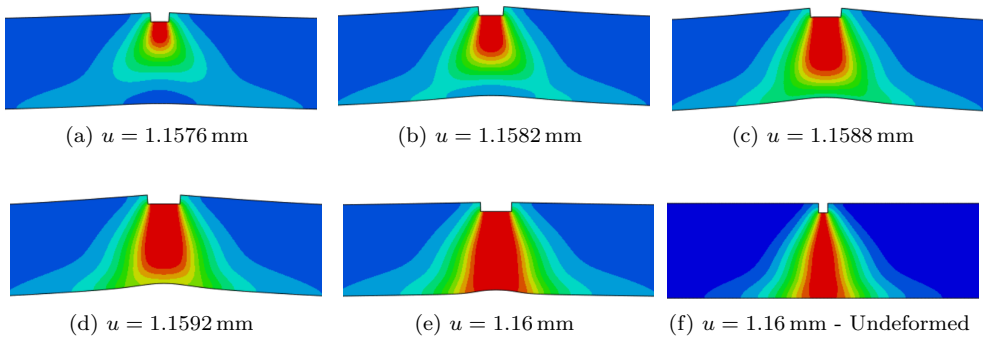

Fig. 10: Crack propagation for the system with thin layer thickness $t = 2$ mm and Young's Modulus ratio $E_1/E_2 = 1$.

Finally, in Figs. 11 and 12, the crack starts from the notch, propagates in the more rigid upper layer until the complete failure when the propagation reaches the end of the lower layer. In the cases with a thin layer stiffer than the substrate in Figs.11-12, the crack band appears narrower w.r.t. Figs. 6-8, because of the immediate failure of the substrate as soon as the upper layer fails. On the contrary, in the cases with E_1/E_2 lower than 1, the crack band is more diffuse and the damaged area involves the entire substrate as represented by the predominant light blue color of the contour plots in Figs. 6c,6d,7c,7d,8c,8d, with respect to the predominant dark blue color in Figs. 11c,11d,12c,12d which indicates an almost undamaged sample apart from the crack band area. The same phenomenon is confirmed also by the displacement-reaction force curves in Fig. 5 which show a loading drop at a higher value of prescribed displacement for the cases with

Young's modulus lower than 1 and an almost simultaneous failure of both the upper and lower layers.

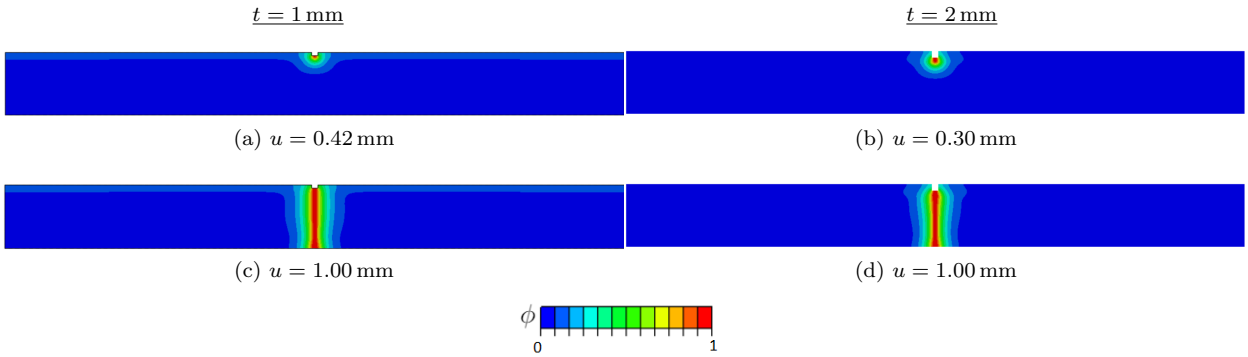

Fig. 11: Crack evolution for Young's Modulus ratio $E_1/E_2 = 10$.

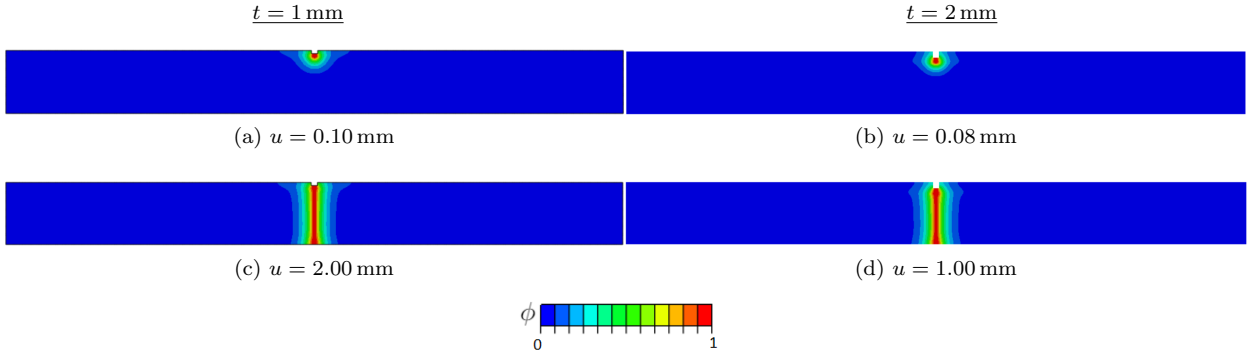

Fig. 12: Crack evolution for Young's Modulus ratio $E_1/E_2 = 100$.

4.1.2. Critical fracture energy influence

The models with upper layer thickness $t = 1\,\text{mm}$ and $t = 2\,\text{mm}$ are chosen to assess the effect of the ratio between the critical energy fracture G_c^b of both constituents. For this purpose, we select varying the value of the top layer G_{c1} and keeping constant the value of $G_{c2} = 10.34\text{N/mm}$ for the lower layer. The system's response for these cases in terms of the evolution of the reaction force vs. the imposed displacement at the ends is shown in Fig. 13. Based on these results, it can be observed that the curves have very similar behavior to each other, distinguished only by the prescribed displacement that causes the complete failure of the joint.

However, if the crack path is analysed (see Figs. 14 -16), it can be seen that the critical fracture energy ratio G_{c1}/G_{c2} influences the failure mechanism. The critical fracture energy ratio $G_{c1}/G_{c2} = 0.01$ brings to the failure of the upper layer only, without the propagation of the crack through the joint thickness (see Fig. 14). For $G_{c1}/G_{c2} = 0.1$, the damage firstly develops within the upper layer, and propagates vertically in a second step (see Fig. 15). This difference is not as visible for $G_{c1}/G_{c2} = 1$ (Fig. 9) as expected since the two layer have the same parameters, as already noticed in the previous section.

It is worth pointing out that the multiple cracks developed in the upper layer in Fig. 14 are more distant among themselves in the case with thickness $t = 2\,\text{mm}$ compared to the case of $t = 1\,\text{mm}$. Considering previous experimental tests on equivalent samples, the displayed numerical results exhibit a solid correlation with the SEM images exhibiting the fracture of the thin gold layer - polymeric substrate specimens performed in [101], which have also been addressed by [102], see Fig. 17.

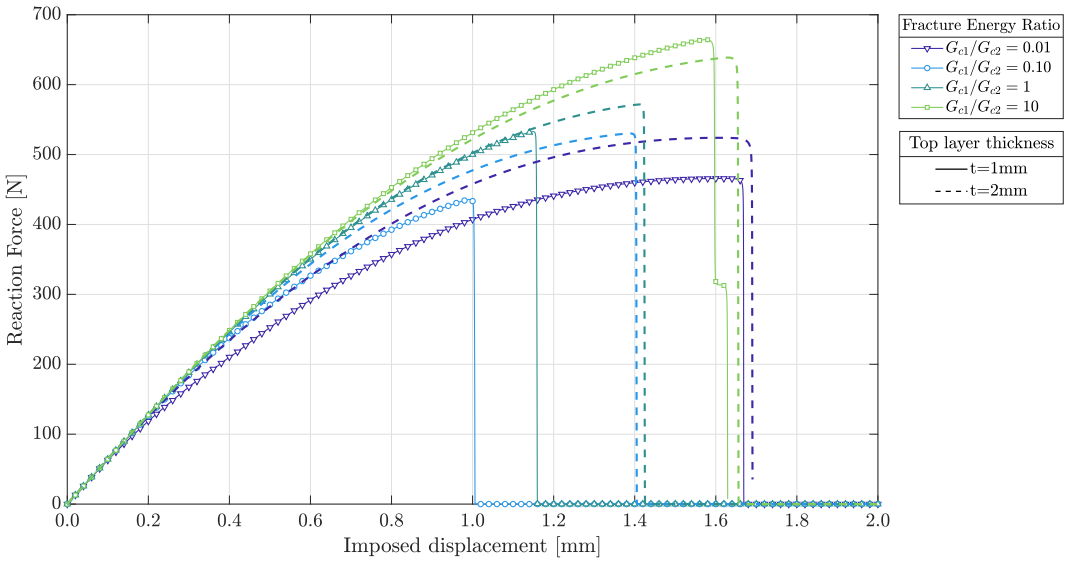

Fig. 13: Parametric study on the effect of critical fracture energy mismatch in a bilayer structure. For the lower layer, the PET material parameters have been used (see Tab. 1), varying the upper layer value of G_{c1}.

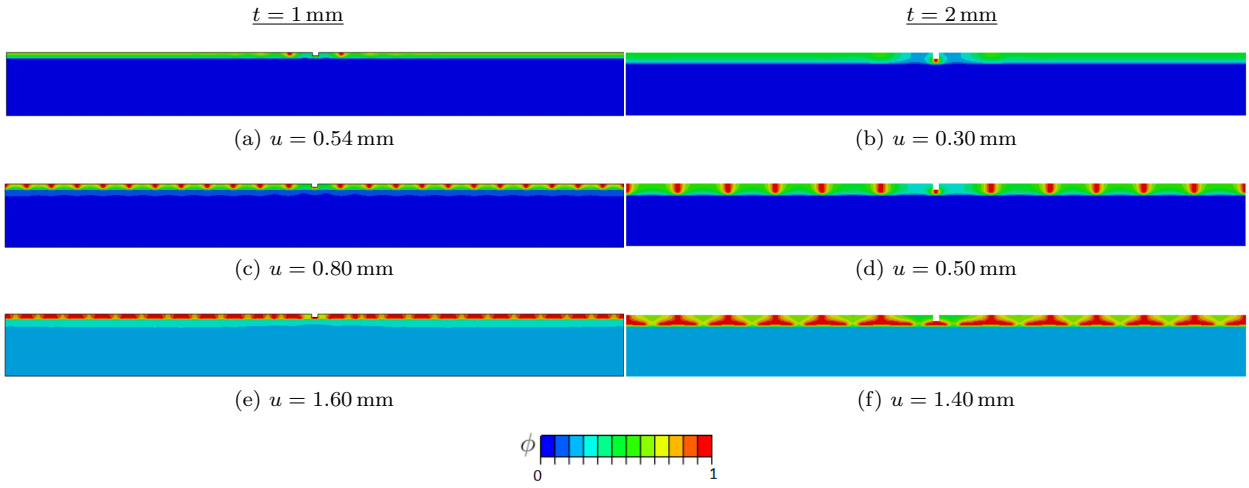

Fig. 14: Crack evolution for the fracture energy ratio $G_{c1}/G_{c2} = 0.01$.

Finally, for $G_{c1}/G_{c2} = 10$, the crack starts in the lower layer, which has a lower value for G_c^b, and propagates into the upper layer later (Fig. 16). This latter case shows a different crack path for the case with $t = 1\,\text{mm}$ and $t = 2\,\text{mm}$ since in the thicker layer model, two symmetrical cracks developed from the bottom edge reach the interface and propagate along it towards the central notch in the upper layer.

The length scale l_0 is computed through the Eq. (12) assuming as input parameter G_c and σ_c. For the simulations presented in previous paragraphs, the length scale has been considered constant, which corresponds to an indirect variation of σ_c according to the given equation.

In order to address a case where σ_c is kept constant, and therefore l_0 is changing, several tests have been conducted to elucidate this possibility. For these numerical runs, the properties in Tab. 2 are employed for the upper layer, keeping the Young Modulus and $\sigma_c = 55\,\text{MPa}$ constant and varying the G_c ratio and

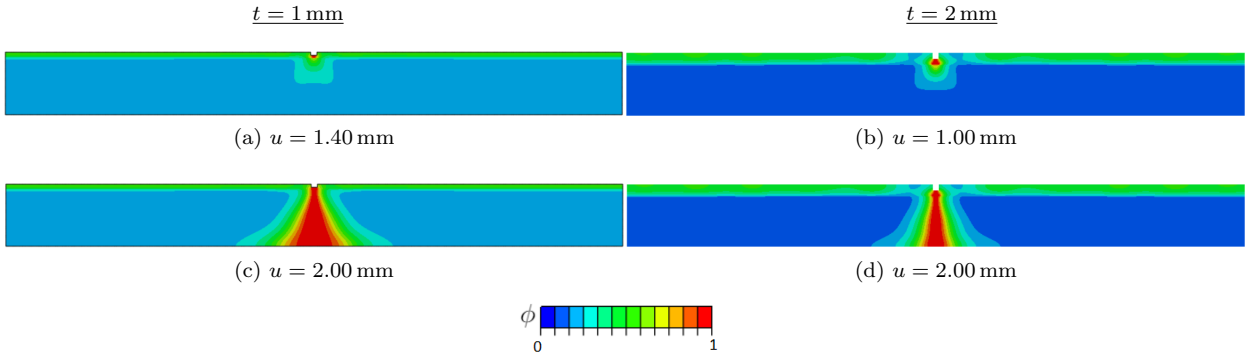

Fig. 15: Crack evolution for the fracture energy ratio $G_{c1}/G_{c2} = 0.1$.

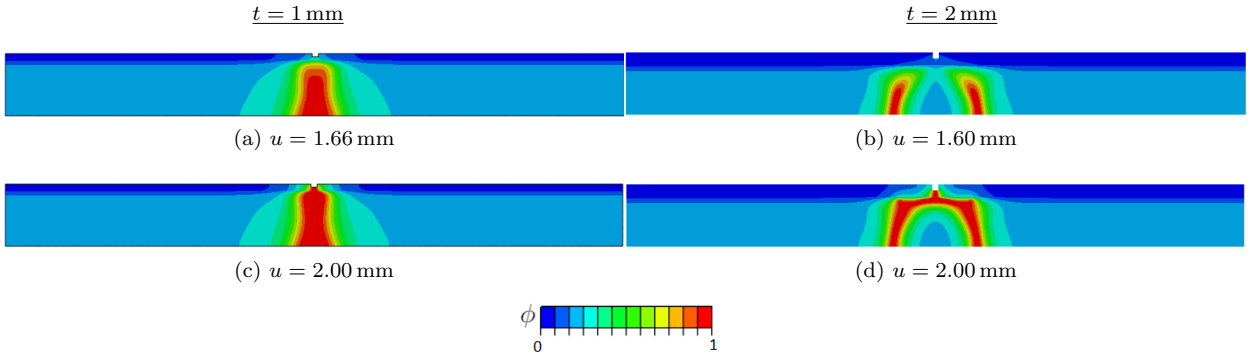

Fig. 16: Crack evolution for the fracture energy ratio $G_{c1}/G_{c2} = 10$.

the length scale parameter accordingly. The results reveal that the fracture pattern does not change for the cases considered in this parametric study compared to the ones shown in Fig. 9, where the crack onset is located in the center of the sample, see Fig. 18 for two examples. The corresponding reaction forces - displacement curves are plotted in Fig. 19.

Material	**E** [GPa]	σ_c [MPa]	$\mathbf{l_0}$ [mm]	$\mathbf{G_c}$ [N/mm]	$\mathbf{G_{c1}/G_{c2}}$
Substrate	2800	55	1.0	10.34	
Test 1	2800	55	10.0	103.4	10
Test 2	2800	55	2.0	20.68	2
Test 3	2800	55	1.0	10.34	1
Test 4	2800	55	0.5	5.17	0.5
Test 5	2800	55	0.1	1.034	0.1

Tab. 2: Mechanical properties of linear elastic materials used for the bilayer plate simulations.

4.2. Thin linear elastic layer on hyperelastic substrate

The present section expands the results obtained in the previous subsection, considering more realistic multi-material joints. In fact, in industrial applications, the components of structural joints do not differ for only one material parameter at a time, but the mismatch regards all the mechanical properties. Hence, in this section, the simulations are carried out considering a polymeric substrate joined to other materials with very different properties.

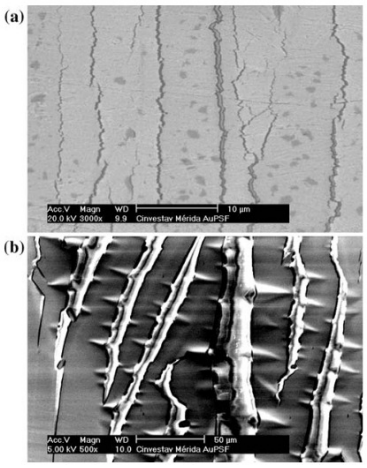

Fig. 17: Multiple cracking of gold films over polymeric PSF substrates. (a) gold layer thickness 50nm and crack spacing $\approx 30\,\mu$m, (b) thickness 200nm and crack spacing. Reused with permission from [101].

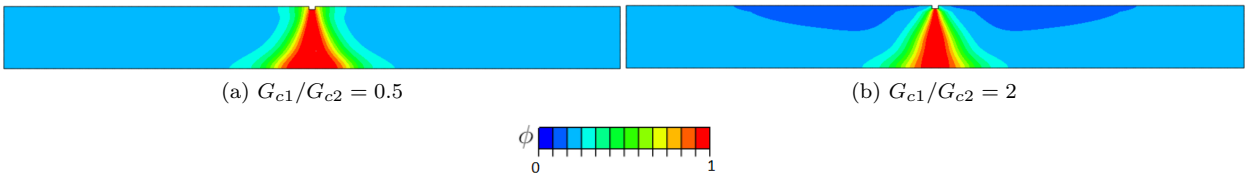

Fig. 18: Crack evolution for Young's Modulus ratio $E_1/E_2 = 0.001$ and different fracture energy ratios.

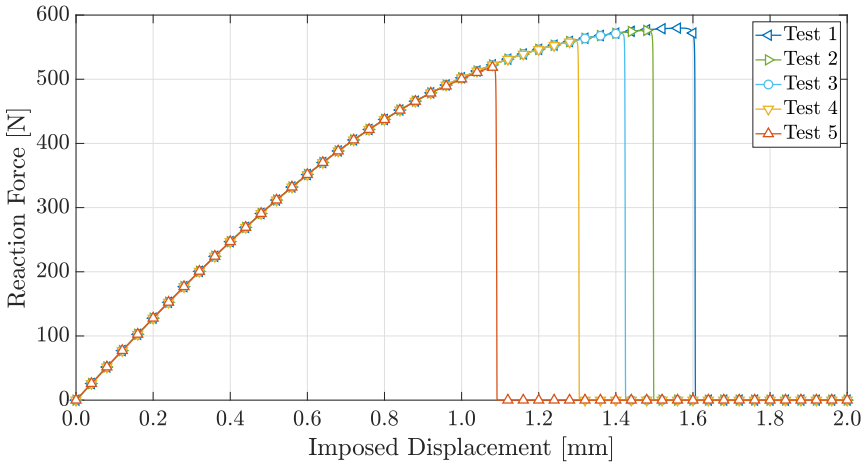

Fig. 19: Reaction forces for different G_c ratios according to Tab. 2.

Compared to the previous section, where the investigation focus on the influence of only one parameter at a time, the simulations here involve layers with different E, ν, G_c and l_0 values. In particular, Tab. 3 reports the mechanical properties of the considered materials: silicone, aluminium and copper. In flexible electronics and solar cells application, the PET polymer is coupled to these materials, and it is more flexible than the linear elastic layer.

For the simulations carried out under plane strain hypothesis, the upper layer is considered linear elastic

Material	E [GPa]	ν	λ [GPa]	μ [GPa]	G_c [N/mm]	σ_c [MPa]	l_0 [mm]	Ref.
PET (substrate)	2.80	0.37	2.91	1.02	10.34	55	1.00	[84, 99]
Aluminium	64	0.33	46.70	24.06	20.00	190	3.73	[103]
Copper	120	0.34	95.15	44.78	0.57	222	0.15	[104]
Silicone	130	0.16	26.37	56.03	0.04	72	0.10	[84]

Tab. 3: Mechanical properties of the materials used for the bilayer plate simulations.

using the Kirchhoff-Saint Venant constitutive law. In contrast, the lower layer is modeled as Neo-Hookean material (see Sec. 2.2 for the difference between these two constitutive models).

The first application considers the coupling of a silicone layer with a PET substrate, using the geometry and boundary conditions shown in Fig. 20. Compared to the previous model, only the materials are different.

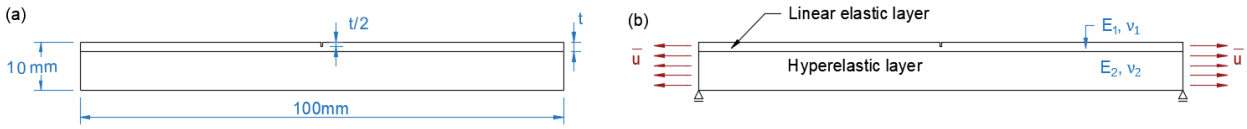

Fig. 20: Geometry (a) and boundary conditions (b) for a bilayer joint with linear elastic and hyperelastic components. The simulations consider $t = 1, 2, 3, 4, 5$ mm.

The influence of the upper layer thickness is shown in Fig. 21. For each simulation, the crack pattern is depicted through different snapshots in Figs. 22, 23 and 24.

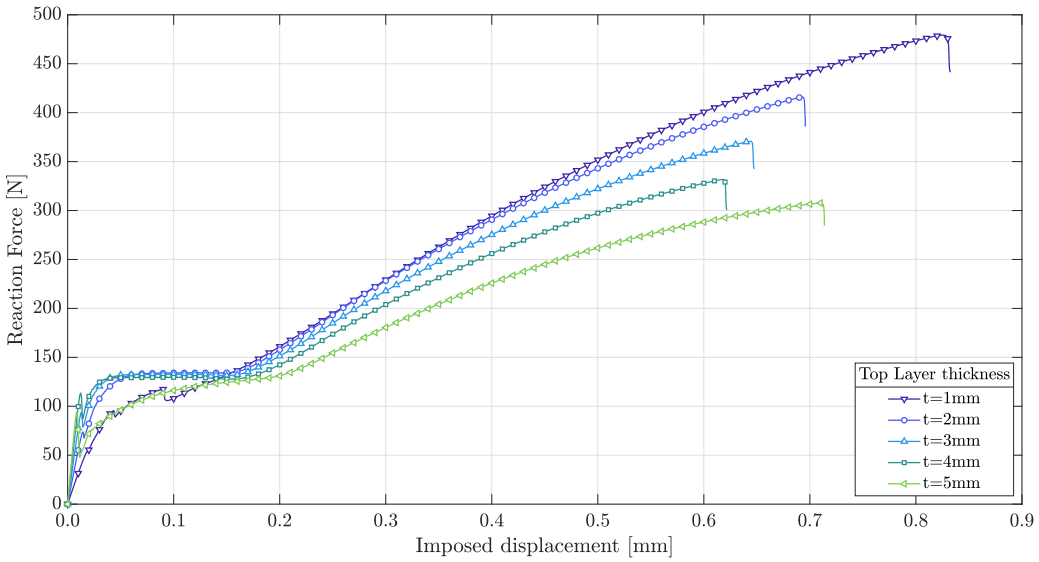

Fig. 21: Thickness influence on the response of a bilayer structure composed by a linear elastic silicone layer (top) and a hyperelastic PET layer (bottom).

For the silicone layer thickness equal to 1 mm, current results predict that the crack starts propagating from the notch and reaches the interface between both components (Fig. 22a). This causes a first drop of the load in the force-displacement curve. With the increase of the applied displacement, while the first one propagates horizontally (Fig. 22b), new equidistant cracks commence at the upper layer in the proximity of the lateral edges, corresponding to other load drops. The phenomenon repeats creating crack pattern

composed by equidistant cracks in the upper layer (Fig. 22c and 22d) until the complete debonding from the substrate (Fig. 22e).

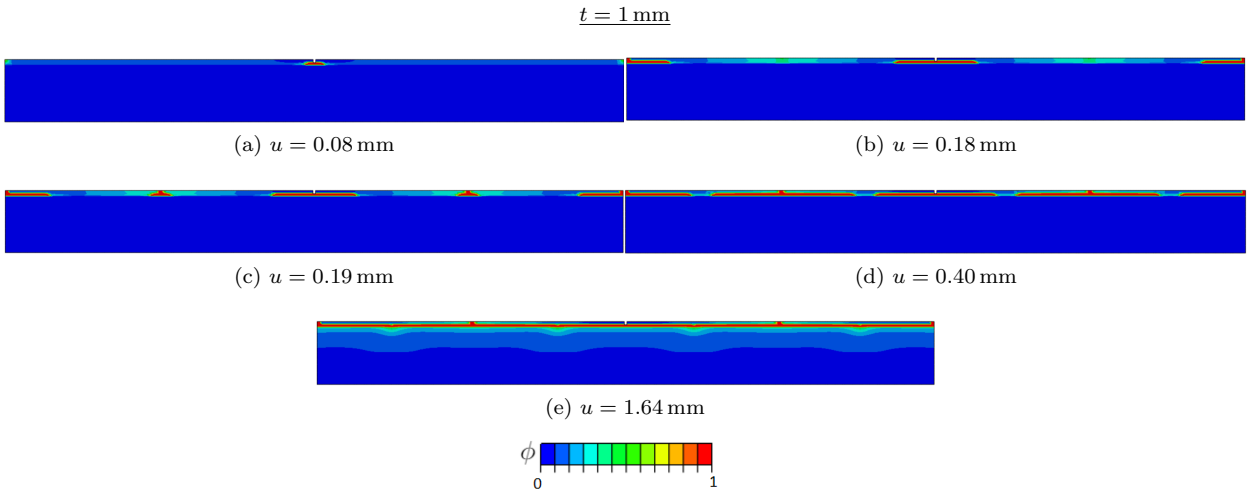

Fig. 22: Crack evolution for the joint composed by the PET substrate and silicone layer of thickness $t = 1\,\text{mm}$.

For thicker silicone layers ($t = 2.0, 3.0, 4.0, 5.0\,\text{mm}$), the crack stemming from the notch firstly propagates vertically within the upper layer, causing a first drop in the relative load-displacement curve. At the interface with the polymeric substrate, the crack is deflected and branches horizontally until the debonding of the substrate, without another initiation of a new crack from the upper edge. The phase-field evolution is very similar to each other for all current the simulations, being depicted in Figs. 23 and 24.

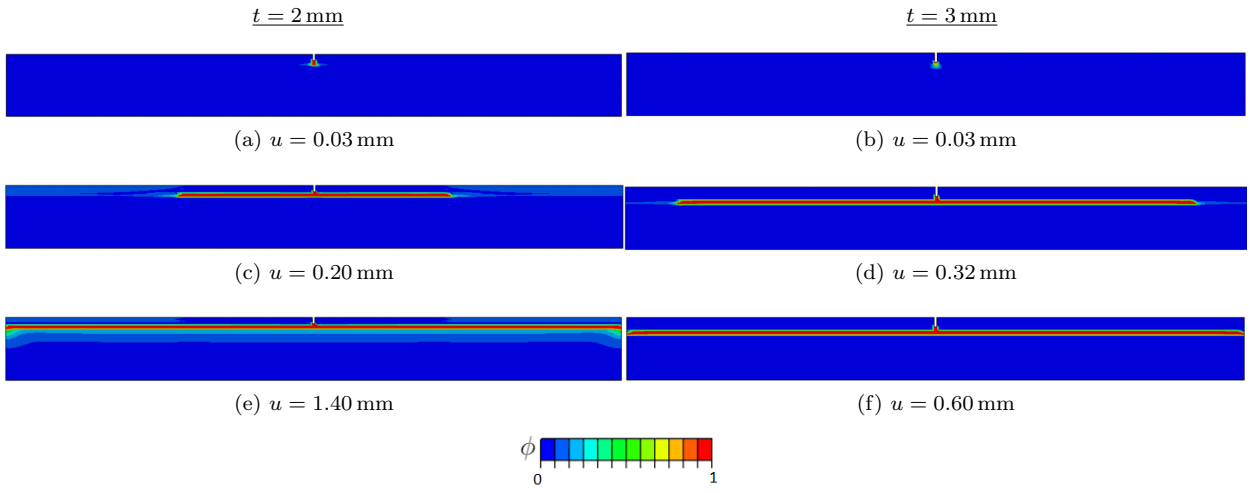

Fig. 23: Crack evolution for the joint composed by the PET substrate and silicone layer with $t = 2.0, 3.0\,\text{mm}$.

The second set of simulations compares the results already obtained for the silicone-PET joint with the response of the same polymeric substrate coupled with thin aluminum and copper layers. The displacement-force curves are shown in Fig. 25 considering the upper layer thickness equal to $t = 1\,\text{mm}$ and $t = 2\,\text{mm}$.

The load-displacement curve for the aluminium layer corresponds to a crack propagation that commences from the notch and propagates vertically through the two layers, as shown in Fig. 26, for both the upper layer thicknesses 1 mm and 2 mm. Moreover, it can be noticed that the failure of the aluminium-PET joint

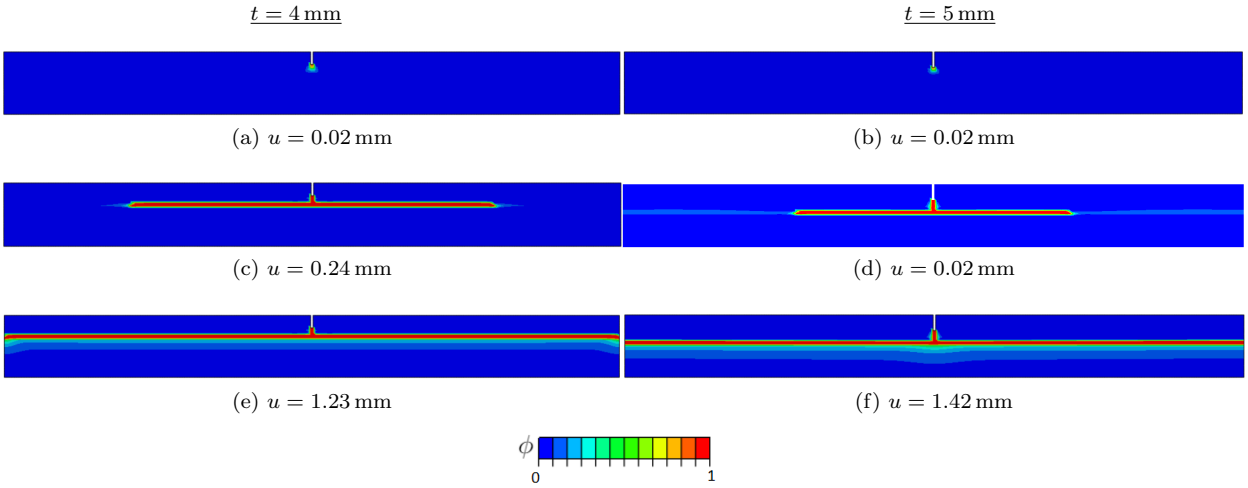

Fig. 24: Crack evolution for the joint composed by the PET substrate and silicone layer with $t = 4.0$, $5.0\,\text{mm}$.

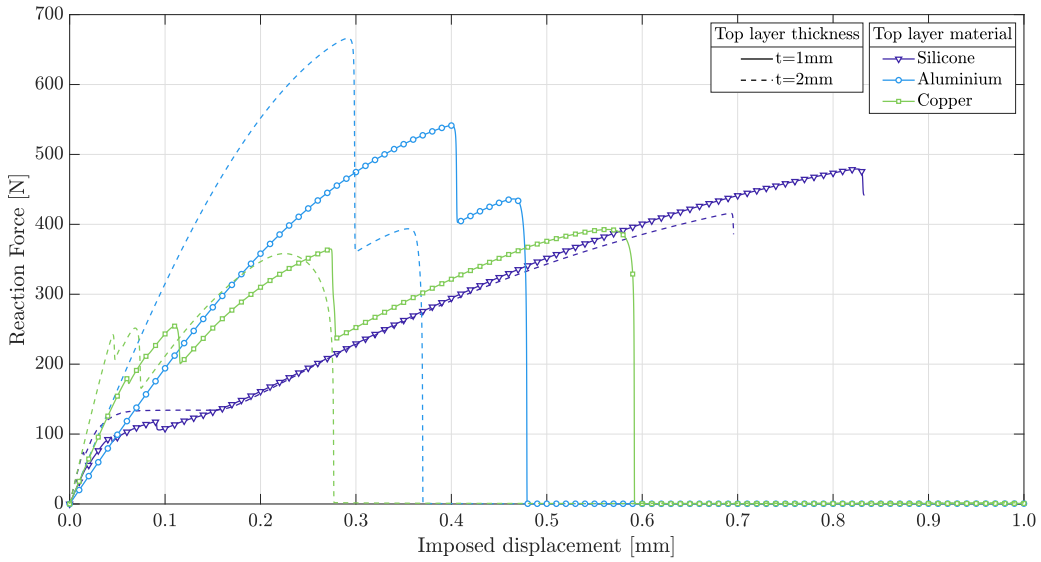

Fig. 25: Thickness and material properties influence on the response of a bilayer structure composed by a PET layer (lower layer, hyperelastic) and different linear elastic layers: aluminium, copper and silicon, with different thicknesses.

.

shows a discontinuity corresponding to the state at which the crack meets the interface in Figs. 26a and 26b, before propagating across it as captured in Figs. 26c and 26e for $t = 1\,\text{mm}$ and in Figs. 26d and 26f for $t = 2\,\text{mm}$.

Analyzing the copper-PET joint crack evolution for the thickness $t = 1\,\text{mm}$, the phase-field evolution shows the formation of cracks equidistant from the notch that grow until the central crack propagates through the interface until the complete failure of the joint (see Fig. 27). Silicone and copper have Young's Modulus of the same order of magnitude, which is reflected in a similar failure mode at the initial stage. However, the different G_{c1}/G_{c2} ratio, equal to $0.57N/mm$ for the copper joint and 0.04N/mm for the silicone, determines the different response since the mismatch for the other mechanical parameters does not reach an order of

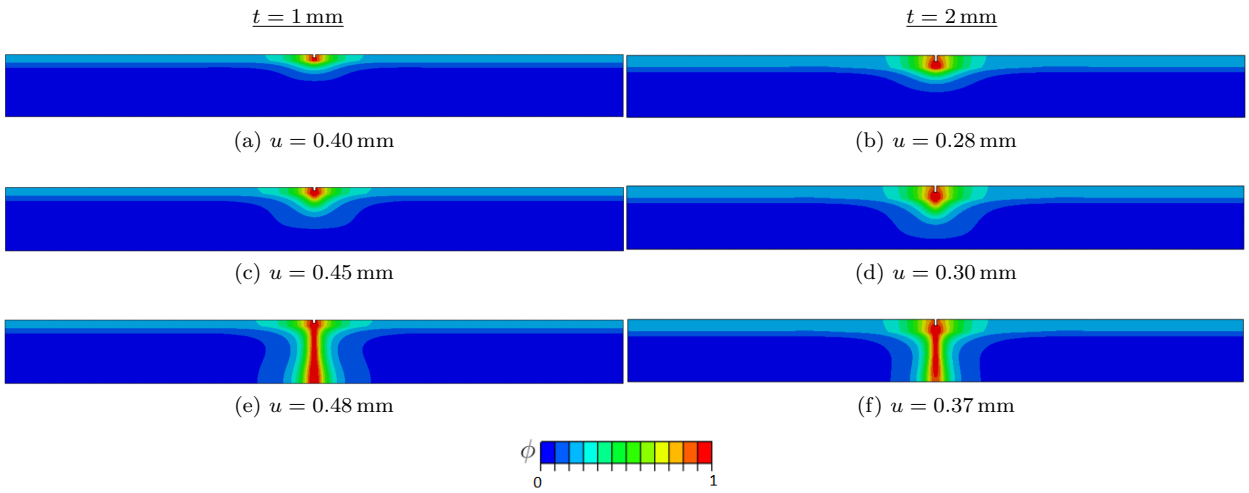

(a) $u = 0.40\,\text{mm}$ (b) $u = 0.28\,\text{mm}$

(c) $u = 0.45\,\text{mm}$ (d) $u = 0.30\,\text{mm}$

(e) $u = 0.48\,\text{mm}$ (f) $u = 0.37\,\text{mm}$

Fig. 26: Crack evolution for the bilayer joint with aluminium layer of thickness $t = 1.0$, $2.0\,\text{mm}$.

magnitude. The thicker case $t = 2\,\text{mm}$, depicted in Fig. 28, starts with a horizontal crack propagation (as in the corresponding silicone case), but the higher critical energy release rate translates into the propagation of the crack in the PET layer and the failure of the joint.

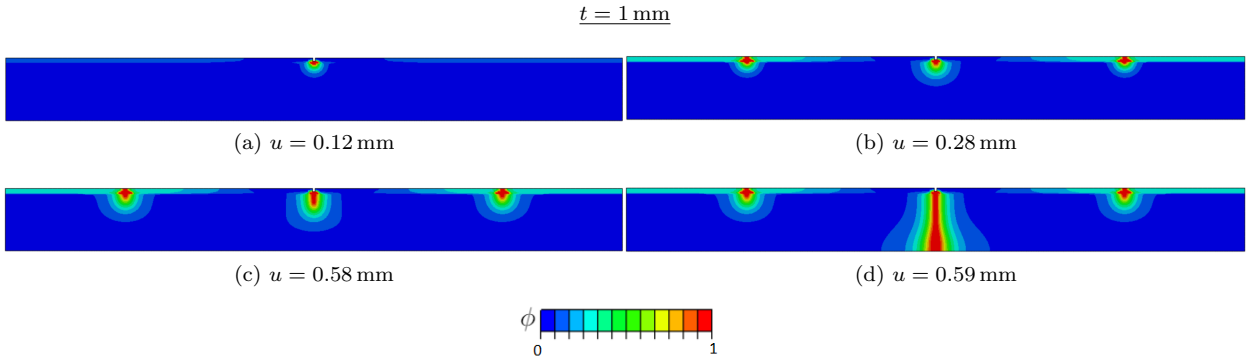

(a) $u = 0.12\,\text{mm}$ (b) $u = 0.28\,\text{mm}$

(c) $u = 0.58\,\text{mm}$ (d) $u = 0.59\,\text{mm}$

Fig. 27: Crack evolution for the bilayer joint with copper layer of thickness $t = 1\,\text{mm}$.

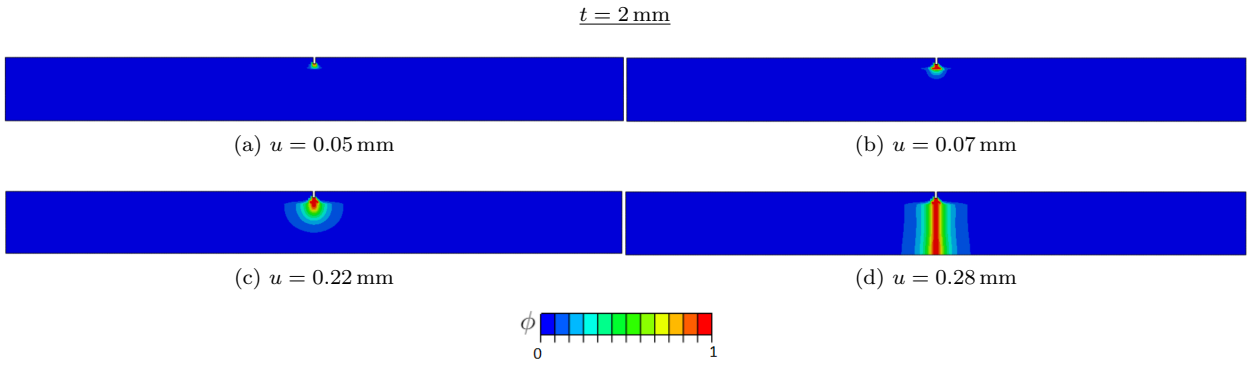

(a) $u = 0.05\,\text{mm}$ (b) $u = 0.07\,\text{mm}$

(c) $u = 0.22\,\text{mm}$ (d) $u = 0.28\,\text{mm}$

Fig. 28: Crack evolution for the bilayer joint with copper layer of thickness $t = 2\,\text{mm}$.

4.3. Interface contribution

In order to address how the fracture simulation is affected by the presence of prescribed interfaces featuring a cohesive-like response, previous simulations are reproduced in the following subsection but with the incorporation of such interfaces separating both material regions. As reported below, this plays an important role in the fracture of the joint, especially in the crack propagation. In line with previous results, parametric studies are conducted by changing both bulk and interface properties: for the bulk, as in the previous section, the Young's Modulus ratio mismatch between both regions; regarding the interface, the critical traction values are changed. For the layers, the same material properties as in the subsection 4.2 have been employed. The thickness of the thin layer is fixed to $t = 1\,\text{mm}$, while the critical interface gaps are set: $g_{nc} = g_{tc} = 1\,\text{mm}$.

The addition of the interface between both layers leads to the competition between crack deflection and propagation as explained in Fig. 29.

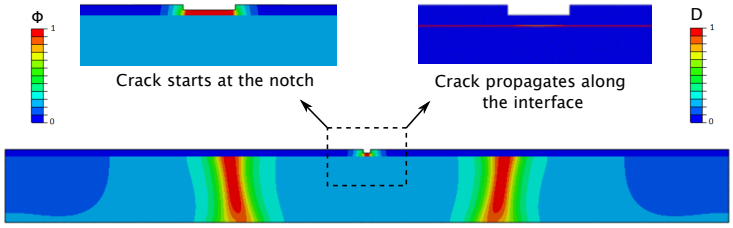

Fig. 29: Details of the crack path and the damage at the interface for the case with $E_1/E_2 = 1$ and $\sigma_c = \tau_c = 0.5\,\text{MPa}$.

The reaction force-displacement curves for Young's Modulus ratio $E_1/E_2 = 1$ are plotted on Fig. 30. It can be deducted that the increase in the critical interface tractions causes a reduction in the final displacement but also a slight increase in the maximum force.

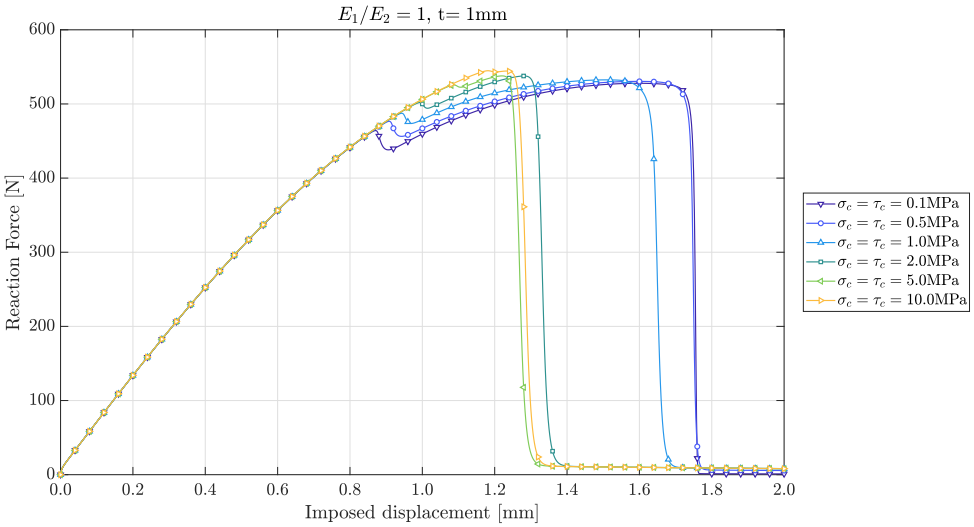

Fig. 30: Reaction force-displacement curves for different cohesive traction values and for Young's Modulus ratio $E_1/E_2 = 1$.

The curves with lower critical tractions ($\sigma_c = \tau_c < 2\,\text{MPa}$) show a step where the force decreases, corresponding to the crack reaching the interface that acts as a barrier. In such scenarios, the interface toughness might determine the cracking mechanism, which is more easily explained with the plots in Fig. 31, where is envisaged the competition between crack deflection and propagation. When a lower strength

characterizes the interface, the crack is deflected for a more significant distance through the interface until it has enough energy to propagate, reaching the extremities when $\sigma_c = \tau_c = 0.1\,\text{MPa}$. The increasing debonding length during the simulation for this case is represented in Fig. 32 in terms of normalized position at the interface vs. damage variable at the interface. The damage evolution is shown at different imposed displacements u.

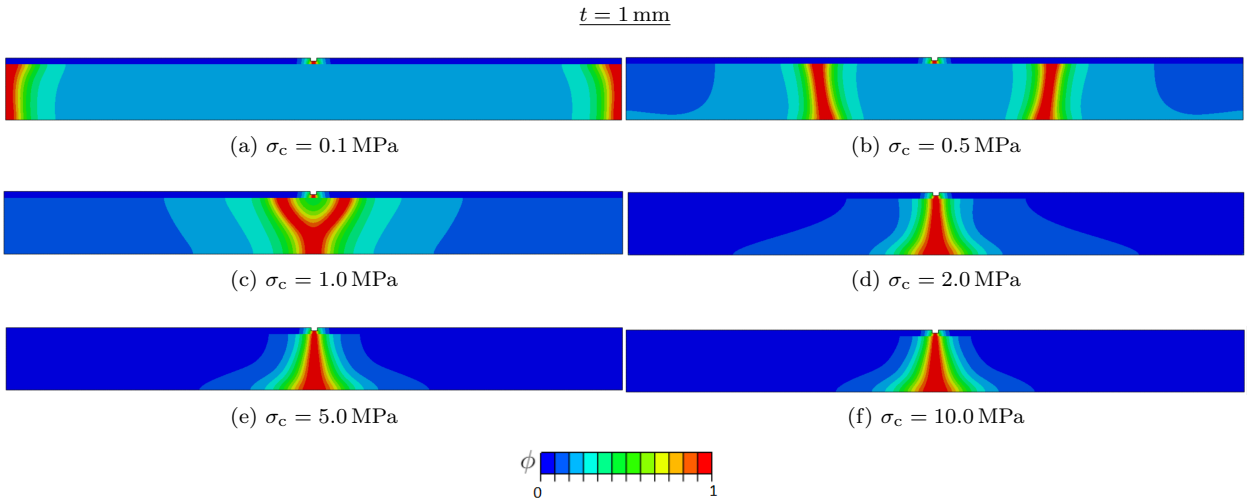

Fig. 31: Crack evolution for different values of the cohesive critical traction σ_c and for layers' Young's Modulus ratio $E_1/E_2 = 1$.

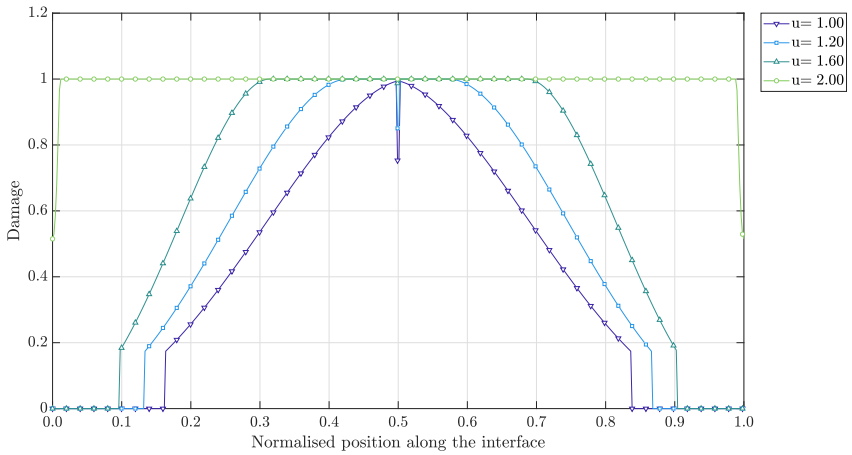

Fig. 32: Damage of the interface at different imposed displacements for the case with $E_1/E_2 = 1$ and $\sigma_c = \tau_c = 0.1\,\text{MPa}$.

However, in cases with $\sigma_c = \tau_c > 2\,\text{MPa}$, the primary mechanism is crack propagation from the upper layer penetrating the bottom layer. Therefore, the delamination length, which can be seen as a second phase in the cracking evolution, is considerably smaller, barely visible in $\sigma_c = \tau_c = 10\,\text{MPa}$ where the interface is not affected at all.

The different debonding lengths corresponding to different values of critical tractions at the final displacement $u = 2$ mm are represented in Fig. 33 in terms of normalised position along the interface vs. damage variable. It can be noticed that lower values of the critical normal and tangential tractions correspond to higher debonding lengths.

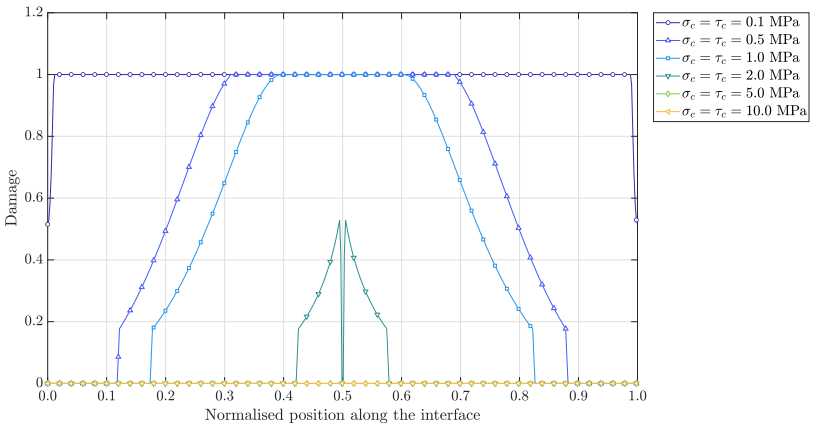

Fig. 33: Damage of the interface at displacement of $u = 2\,\text{mm}$ for the cases with $E_1/E_2 = 1$.

By changing the Young's Modulus ratio to $E_1/E_2 = 5$, it can be seen at the reaction force-displacement curves plotted in Fig. 34 that the difference in terms of maximum displacement is increased between probes whose primary mechanism of fracture is crack propagation and those with crack deflection, having the latter ones a slight decrease in this parameter. Taking a look at the damage plots in Fig. 35, the same pattern as before is observed: lower critical traction in the interface is associated with more deflection.

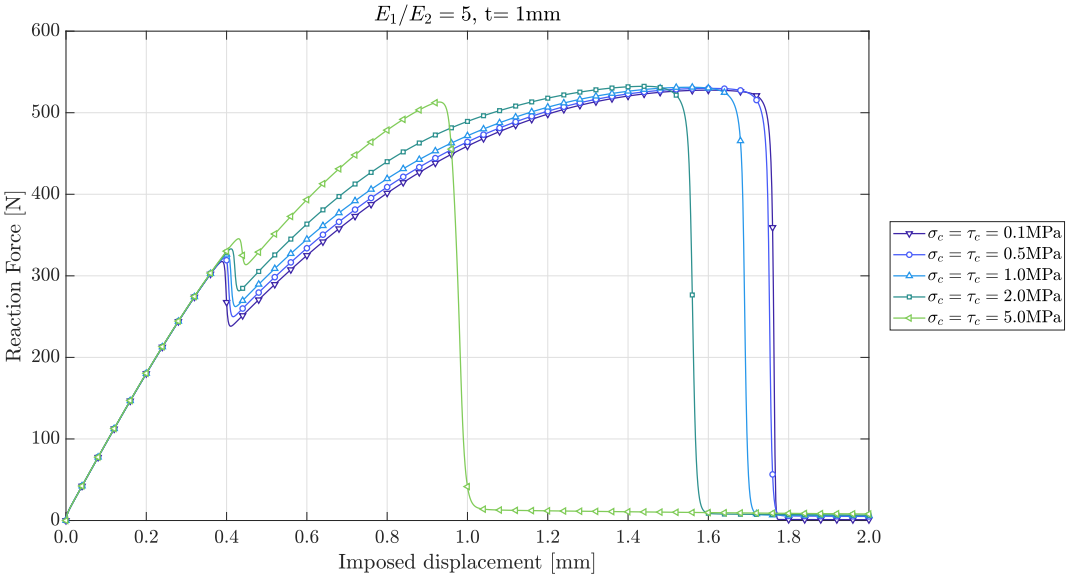

Fig. 34: Reaction force-displacement curves for different cohesive traction values and for Young's Modulus ratio $E_1/E_2 = 5$.

Finally, the reaction force-displacement curves for $E_1/E_2 = 10$ are plotted in Fig. 36 and the associated phase-field isocontour plots in Fig. 37. They show the same mechanical behaviour when changing interface properties as with the previous probes of this section.

4.4. Ceramic Islands

For this last subsection, the proposed analysis is examined against practical applications that concern ceramic islands disposed periodically on a polyimide (PI) substrate (Fig. 38), see [3]. This series of tests

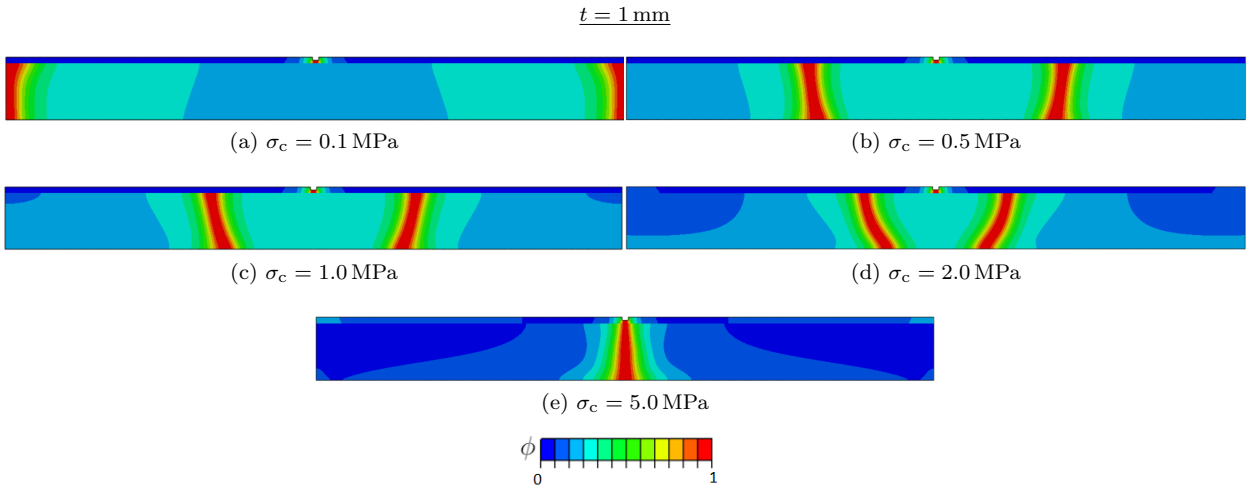

Fig. 35: Crack evolution for different values of the cohesive critical traction σ_c and for Young's Modulus ratio $E_1/E_2 = 5$.

consists of the horizontal pulling of these structures to address how the mechanism of failure was affected by the dimension of the island, being the experimental results of this study published in Fig. 39, where it is seen that bigger thickness or smaller island size is associated to a fracture mechanism of crack debonding. In this plot, at the frame, the size and thickness of the island will be considered within this approach. It is worth highlighting that these structures have been approximated with a plane-strain configuration, like in [3, 105], and that a CZM analysis in 3D for this example has been tackled by Reinoso et al. [106] to simulate cohesive fracture.

For this numerical analysis, one ceramic island is considered with the dimensions that are displayed in Tab. 4 and the geometry in Fig. 40. These numerical samples intend to replicate the fracture results with those obtained experimentally. The materials employed for both layers are listed in Tab. 5. The parametric study is performed by changing: (i) the island thickness, (ii) the critical interface tractions, and (iii) the critical interface gaps.

Island size	L	$20\,\mu$m
Island thickness	h	$0.1 - 0.3 - 0.5\,\mu$m
Substrate size	S	$30\,\mu$m
Substrate height	H	$7.5\,\mu$m

Tab. 4: Dimensions used for the simulations regarding ceramic islands on polymeric substrate.

		E [MPa]	ν	G_c^b [N/mm]	l_0 [μm]
Island	Linear Elastic	200000	0.3	0.1	0.1
Substrate	Hyperelastic	9200	0.3	10	0.1

Tab. 5: Mechanical properties used for the simulations regarding ceramic islands on polymeric substrate, taken from [3].

The simulations results are summarized in Tab. 6 for each configuration and interface properties and referred to the same imposed displacement. According to the maximum values reached by the phase-field and the damage variables, the failure mechanism has been classified as cracking ($\phi_{max} \geq 0.9$), debonding ($D_{max} \geq 0.9$), or Mixed Mode ($\phi_{max} \geq 0.9$ and $D_{max} \geq 0.9$).

All the cases with the thinnest ceramic layer ($0.1\,\mu$m) result in cracking, with only some of them experiencing subsequent debonding. An example of the debonding failure mechanism is shown in Fig. 41a, while the Mixed Mode failure is plotted in Fig. 41b.

The configuration having the ceramic layer thickness equal to $0.3\,\mu$m exhibits all the possible failure

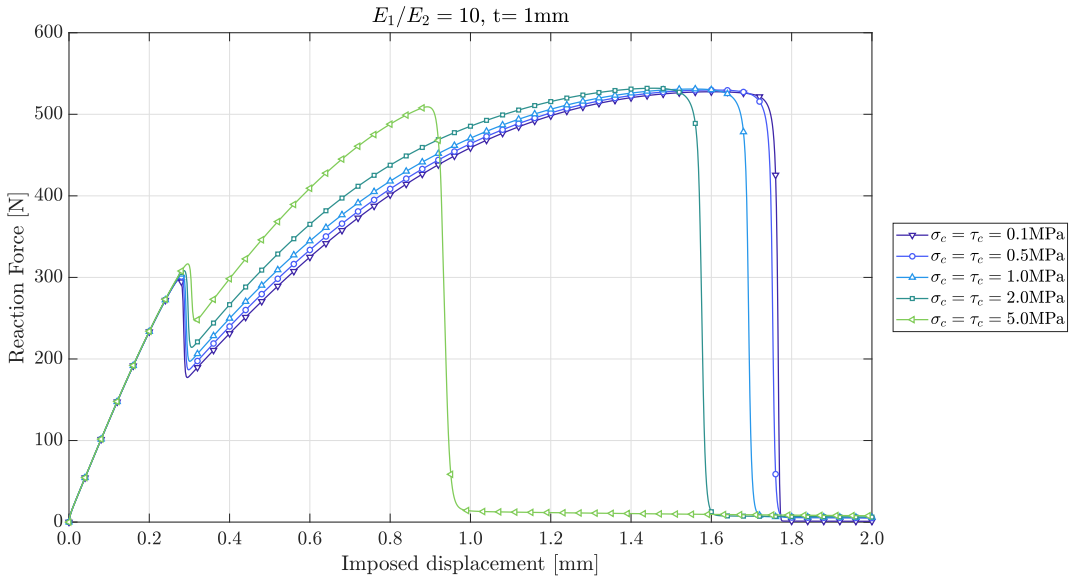

Fig. 36: Reaction force-displacement curves for different cohesive traction values and for Young's Modulus ratio $E_1/E_2 = 10$.

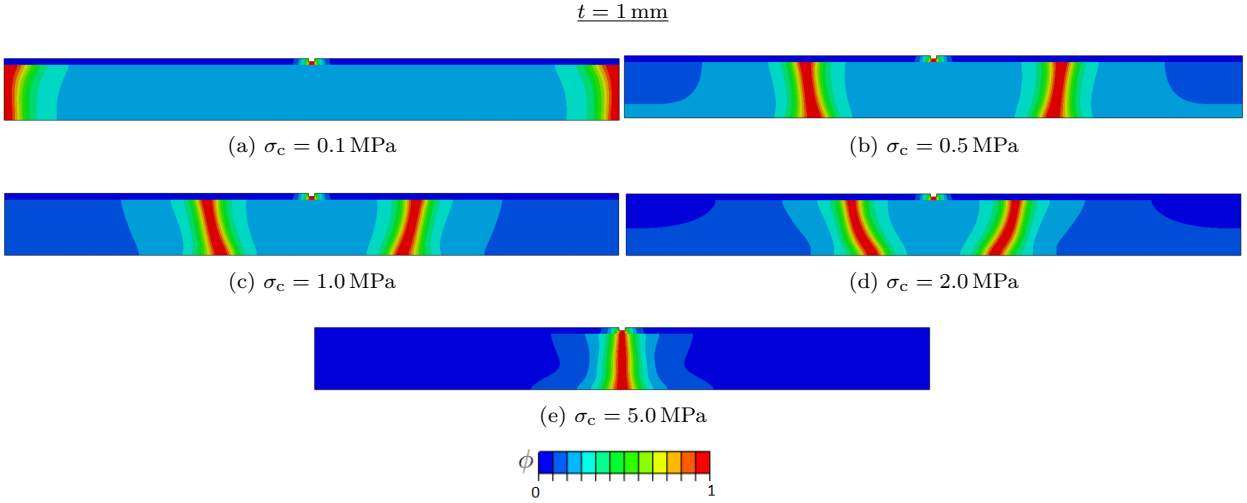

Fig. 37: Crack evolution for different values of the cohesive critical traction σ_c and for Young's Modulus ratio $E_1/E_2 = 10$.

mechanisms. In particular, the configurations with the minimum value of critical traction, $\sigma_c = \tau_c = 1$ MPa, display uniquely delamination at the interface, while the cases with the highest traction values also experience cracking of the upper layer. In these last samples, the values of the critical gaps assume a determinant role to distinguish between only cracking or Mixed Mode failure. The thickest ceramic layer ($0.5\,\mu$m) displays a predominant debonding mechanism of failure. This pattern of failure is displayed in detail in Fig. 42.

In summary, it can be stated from current results that by increasing the thickness of the island, the failure mechanism switches from mainly crack propagation in the layer to debonding of the interface, being this result in accordance with the experimental results from Fig. 39.

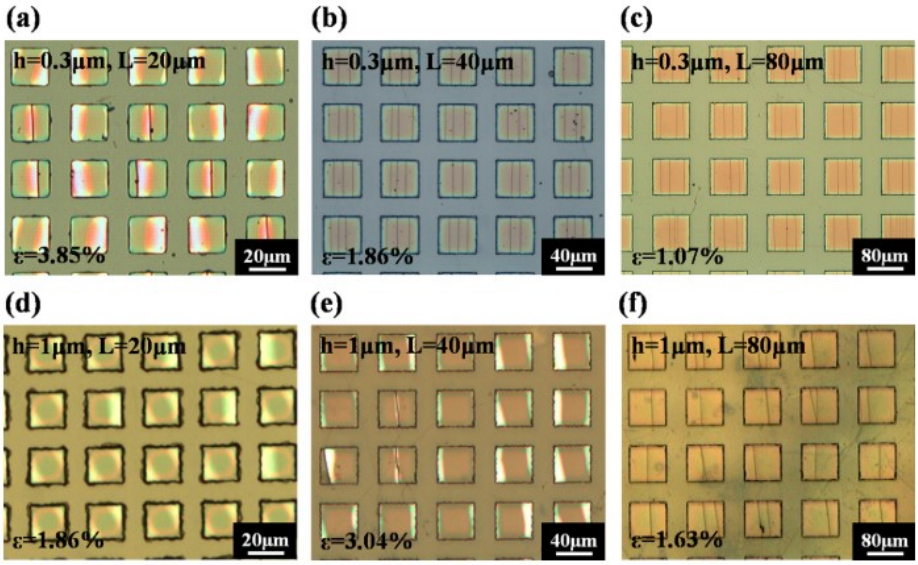

Fig. 38: Ceramic islands (size L and thickness h) on PI (polyimide) substrate stretched horizontally. Source [3].

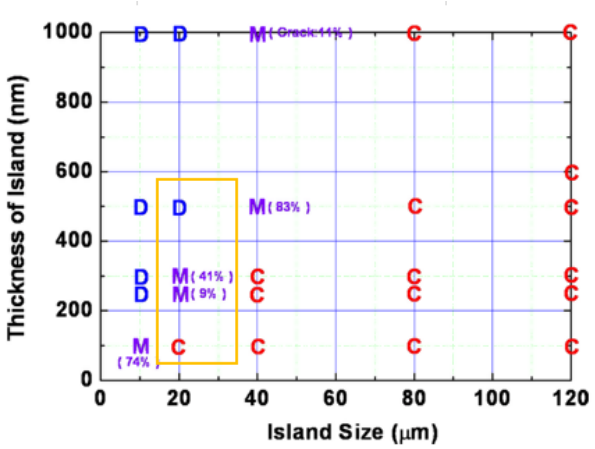

Fig. 39: Experimental failure mechanisms for different islands configurations. C - only cracking occurs, D - only debonding, M - Mixed Mode failure. The results highlighted by the yellow rectangle correspond to the cases simulated in this work. Adapted from [3].

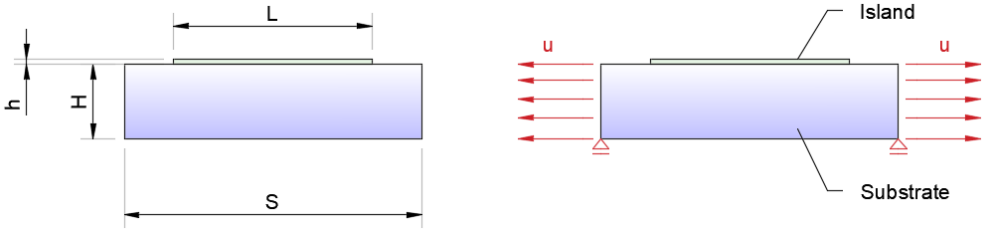

Fig. 40: Geometry and boundary conditions used for the simulations regarding ceramic islands on polymeric substrate.

5. Final remarks

Fracture simulation in joint structures with rubber-like materials has been studied through a phase-field approach for hyperelastic materials. The phase-field approach has been formulated in the framework of

Experimental result [3]	Island thickness	$\sigma_c = \tau_c$ [MPa]	$g_{tc} = g_{nc}$ [μm]		
			0.05	0.1	0.2
Cracking	0.1 μm	1	Mixed Mode Failure $\phi_{max} = 1$; $D_{max} = 1$	Mixed Mode Failure $\phi_{max} = 1$; $D_{max} = 0.9$	Cracking $\phi_{max} = 1$; $D_{max} = 0$
		2	Mixed Mode Failure $\phi_{max} = 1$; $D_{max} = 0.9$	Cracking $\phi_{max} = 1$; $D_{max} = 0.45$	Cracking $\phi_{max} = 1$; $D_{max} = 0.2$
		3	Cracking $\phi_{max} = 1$; $D_{max} = 0.3$	Cracking $\phi_{max} = 1$; $D_{max} = 0.3$	Cracking $\phi_{max} = 1$; $D_{max} = 0$
Mixed	0.3 μm	1	Debonding $\phi_{max} = 0.07$; $D_{max} = 1$	Debonding $\phi_{max} = 0.08$; $D_{max} = 1$	Debonding $\phi_{max} = 0.09$; $D_{max} = 1$
		2	Mixed Mode Failure $\phi_{max} = 1$; $D_{max} = 1$	Cracking $\phi_{max} = 1$; $D_{max} = 0.47$	Cracking $\phi_{max} = 1$; $D_{max} = 0.22$
		3	Mixed Mode Failure $\phi_{max} = 1$; $D_{max} = 1$	Cracking $\phi_{max} = 1$; $D_{max} = 0$	Cracking $\phi_{max} = 1$; $D_{max} = 0.17$
Debonding	0.5 μm	1	Debonding $\phi_{max} = 0.03$; $D_{max} = 1$	Debonding $\phi_{max} = 0.03$; $D_{max} = 1$	Debonding $\phi_{max} = 0.03$; $D_{max} = 1$
		2	Debonding $\phi_{max} = 0.1$; $D_{max} = 1$	Debonding $\phi_{max} = 0.1$; $D_{max} = 1$	Debonding $\phi_{max} = 0.1$; $D_{max} = 1$
		3	Mixed Mode Failure $\phi_{max} = 1$; $D_{max} = 1$	Mixed Mode Failure $\phi_{max} = 1$; $D_{max} = 1$	Mixed Mode Failure $\phi_{max} = 1$; $D_{max} = 1$

Tab. 6: Simulated failure mechanisms according to the interface properties for different values of island thickness.

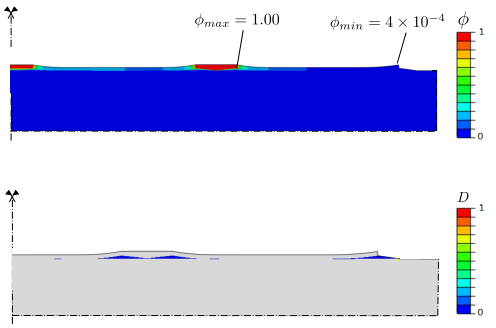

(a) Cracking failure of the island obtained with $\sigma_c = \tau_c = 1$ MPa and $g_{tc} = g_{nc} = 0.2\,\mu$m

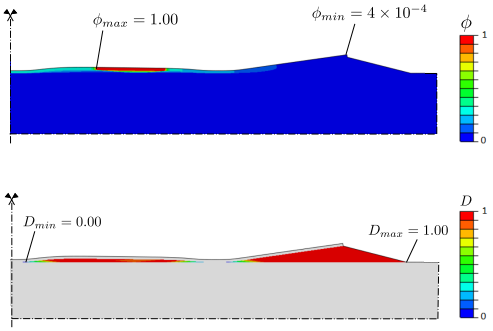

(b) Mixed mode failure of the island obtained with $\sigma_c = \tau_c = 1$ MPa and $g_{tc} = g_{nc} = 0.05\,\mu$m

Fig. 41: Details of the failure mechanisms for cases with ceramic layer thickness equal to 0.1 μm, which show cracking and mixed-mode fracture, respectively. Phase-field isocontours in the top figures and interface damage in the bottom ones. For visualization purpose, the deformation has been magnified by a factor of 15.

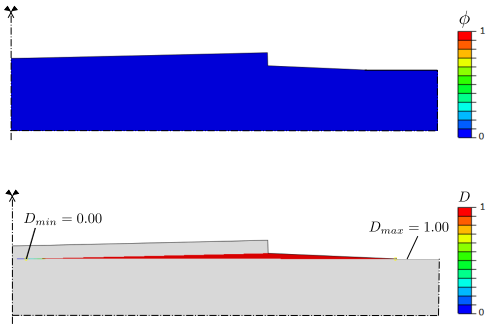

Fig. 42: Details of the ceramic island layer for the case with thickness 0.5 μm in the case of only debonding. Obtained with $\sigma_c = \tau_c = 1$ MPa and $g_{tc} = g_{nc} = 0.05\,\mu$m. Phase-field isocontours in the top figure and interface damage in the lower one. For visualization purpose, the deformation has been magnified by a factor of 15.

finite elasticity and used to study the effect of material properties mismatch on the crack propagation in bilayered structures.

Moreover, the framework has been enriched by considering the existence of imperfect interfaces between the joint components modeled using the CZM, providing a plausible tool of interest in industrial uses. The employed framework has been applied in various numerical examples; among the most important conducted analyses, the dependence on the material (ceramic, polymer, metal) of the thin layer, and the competition between crack propagation in the bulk and delamination at the interface have been addressed within thin layer-flexible substrate systems.

Although the phase-field approach already captures the crack propagation at the interface in some configurations, the coupling with CZM provides a better insight into the different failure mechanisms and in particular, into the accuracy of the simulations for Mixed Mode failure.

Future investigation of this computational framework will be dedicated to couple the phase-field damage for both the bulk and the interface considering two damage fields to model the interface state. In addition to this, an extension to structured interfaces is desired, with the possibility of combining the PF-CZM numerical approach with experimental testing that validates the work.

6. Acknowledgements

MP and MRM would like to acknowledge support from MIUR to the project of national interest (PRIN 2017) XFAST-SIMS "Extra fast and accurate simulation of complex structural systems" (GA n. 20173C478N). AVG acknowledges the financial support from Erasmus+ funding (Project 2020-1-IT02-KA103-078114) for his visiting time in University of Seville during the period 15/06-15/09 2021. JR acknowledges to the Conserjería de Economía y Conocimiento of the Junta de Andalucía (Spain) for financial support under the projects US-1265577 and P20-00595 and the support of the project PID2019-109723GB-I0 funded by the Spanish Ministry of Science and Innovation.

References

[1] T. Li, Z. Huang, Z. Suo, S. P. Lacour, S. Wagner, Stretchability of thin metal films on elastomer substrates, Applied Physics Letters 85 (16) (2004) 3435–3437. doi:10.1063/1.1806275.

[2] T. Li, Z. Zhang, B. Michaux, Competing failure mechanisms of thin metal films on polymer substrates under tension, THEORETICAL & APPLIED MECHANICS LETTERS 1 (2011) 41002. doi:10.1063/2.1104102.

[3] J. Y. Sun, N. Lu, J. Yoon, K. H. Oh, Z. Suo, J. J. Vlassak, Debonding and fracture of ceramic islands on polymer substrates, Journal of Applied Physics 111 (1) (2012) 103519. doi:10.1063/1.3673805.

[4] G. R. Irwin, Analysis of Stresses and Strains Near the End of a Crack Traversing a Plate, Journal of Applied Mechanics 24 (3) (1957) 361–364. doi:10.1115/1.4011547.

[5] J. W. Hutchinson, Z. Suo, Mixed Mode Cracking in Layered Materials, Advances in Applied Mechanics 29 (C) (1991) 63–191. doi:10.1016/S0065-2156(08)70164-9.

[6] J. R. Rice, A Path Independent Integral and the Approximate Analysis of Strain Concentration by Notches and Cracks, Journal of Applied Mechanics 35 (2) (1968) 379–386. doi:10.1115/1.3601206.

[7] R. Krueger, Virtual crack closure technique: History, approach, and applications, Applied Mechanics Reviews 57 (2) (2004) 109–143. doi:10.1115/1.1595677.

[8] N. Moës, J. Dolbow, T. Belytschko, A finite element method for crack growth without remeshing, International Journal for Numerical Methods in Engineering 46 (1) (1999) 131–150. doi:10.1002/(SICI)1097-0207(19990910)46:1¡131::AID-NME726¿3.0.CO;2-J.

[9] T. Belytschko, T. Black, Elastic crack growth in finite elements with minimal remeshing, International Journal for Numerical Methods in Engineering 45 (5) (1999) 601–620. doi:10.1002/(SICI)1097-0207(19990620)45:5¡601::AID-NME598¿3.0.CO;2-S.

[10] A. Yazid, N. Abdelkader, H. Abdelmadjid, A state-of-the-art review of the X-FEM for computational fracture mechanics, Applied Mathematical Modelling 33 (12) (2009) 4269–4282. doi:10.1016/j.apm.2009.02.010.

[11] G.-H. Shi, Manifold method of material analysis, Tech. rep., Army Research Office Research Triangle Park NC (1992).

[12] G. Ma, X. An, L. He, The numerical manifold method: A Review, International Journal of Computational Methods 7 (1) (2010) 1–32. doi:10.1142/S0219876210002040.

[13] H. Zheng, Y. Yang, G. Shi, Reformulation of dynamic crack propagation using the numerical manifold method, Engineering Analysis with Boundary Elements 105 (February) (2019) 279–295. doi:10.1016/j.enganabound.2019.04.023.

[14] Y. Yang, X. Tang, H. Zheng, Q. Liu, Z. Liu, Hydraulic fracturing modeling using the enriched numerical manifold method, Applied Mathematical Modelling 53 (2018) 462–486. doi:10.1016/j.apm.2017.09.024.

[15] Y. Yang, G. Sun, H. Zheng, C. Yan, An improved numerical manifold method with multiple layers of mathematical cover systems for the stability analysis of soil-rock-mixture slopes, Engineering Geology 264 (2020) 105373. doi:10.1016/j.enggeo.2019.105373.
[16] Y. Yang, D. Xu, F. Liu, H. Zheng, Modeling the entire progressive failure process of rock slopes using a strength-based criterion, Computers and Geotechnics 126 (June) (2020) 103726. doi:10.1016/j.compgeo.2020.103726.
[17] Y. Yang, W. Wu, H. Zheng, Stability analysis of slopes using the vector sum numerical manifold method, Bulletin of Engineering Geology and the Environment 80 (1) (2021) 345–352. doi:10.1007/s10064-020-01903-x.
[18] Z. P. Bazant, G. Pijaudier-Cabot, Nonlocal continuum damage, localization instability and convergence, American Society of Mechanical Engineers (Paper) 26 (88) (1988). doi:10.1016/0148-9062(89)90740-7.
[19] J. Lemaitre, R. Desmorat, Engineering Damage Mechanics, Springer-Verlag, Berlin/Heidelberg, 2005. doi:10.1007/b138882.
[20] P. Areias, M. A. Msekh, T. Rabczuk, Damage and fracture algorithm using the screened Poisson equation and local remeshing, Engineering Fracture Mechanics 158 (2016) 116–143. doi:10.1016/J.ENGFRACMECH.2015.10.042.
[21] R. H. Peerlings, M. G. Geers, R. De Borst, W. A. Brekelmans, A critical comparison of nonlocal and gradient-enhanced softening continua, International Journal of Solids and Structures 38 (44-45) (2001) 7723–7746. doi:10.1016/S0020-7683(01)00087-7.
[22] T. Waffenschmidt, C. Polindara, A. Menzel, S. Blanco, A gradient-enhanced large-deformation continuum damage model for fibre-reinforced materials, Computer Methods in Applied Mechanics and Engineering 268 (2014) 801–842. doi:10.1016/j.cma.2013.10.013.
[23] M. K. Rausch, G. P. Sugerman, S. Kakaletsis, B. Dortdivanlioglu, Hyper-viscoelastic damage modeling of whole blood clot under large deformation, Biomechanics and Modeling in Mechanobiology 20 (5) (2021) 1645–1657. doi:10.1007/s10237-021-01467-z.
[24] G. Barenblatt, The Mathematical Theory of Equilibrium Cracks in Brittle Fracture, in: Advances in Applied Mechanics, Vol. 7, Elsevier, 1962, pp. 55–129. doi:10.1016/S0065-2156(08)70121-2.
[25] D. S. Dugdale, Yielding of steel sheets containing slits, Journal of the Mechanics and Physics of Solids 8 (2) (1960) 100–104. doi:10.1016/0022-5096(60)90013-2.
[26] P. Cornetti, M. Corrado, L. D. Lorenzis, A. Carpinteri, An analytical cohesive crack modeling approach to the edge debonding failure of FRP-plated beams, International Journal of Solids and Structures 53 (2015) 92–106. doi:10.1016/j.ijsolstr.2014.10.017.
[27] K. Park, G. H. Paulino, Cohesive zone models: A critical review of traction-separation relationships across fracture surfaces, Applied Mechanics Reviews 64 (6) (2011). doi:10.1115/1.4023110.
[28] M. Corrado, J. F. Molinari, Effects of residual stresses on the tensile fatigue behavior of concrete, Cement and Concrete Research 89 (2016) 206–219. doi:10.1016/j.cemconres.2016.08.014.
[29] A. Infuso, M. Corrado, M. Paggi, Image analysis of polycrystalline solar cells and modelling of intergranular and transgranular cracking, Journal of the European Ceramic Society 34 (11) (2014) 2713–2722. doi:10.1016/j.jeurceramsoc.2013.12.051.
[30] A. Turon, E. V. González, C. Sarrado, G. Guillamet, P. Maimí, Accurate simulation of delamination under mixed-mode loading using a cohesive model with a mode-dependent penalty stiffness, Composite Structures 184 (2018) 506–511. doi:10.1016/J.COMPSTRUCT.2017.10.017.
[31] G. Alfano, M. A. Crisfield, Finite element interface models for the delamination analysis of laminated composites: mechanical and computational issues, International Journal for Numerical Methods in Engineering 50 (7) (2001) 1701–1736. doi:10.1002/NME.93.
[32] L. García-Guzmán, J. Reinoso, A. Valverde-González, E. Martínez-Pañeda, L. Távara, Numerical study of interface cracking in composite structures using a novel geometrically nonlinear linear elastic brittle interface model: Mixed-mode fracture conditions and application to structured interfaces, Composite Structures 248 (2020) 112495. doi:https://doi.org/10.1016/j.compstruct.2020.112495.
[33] J. Williams, H. Hadavinia, Analytical solutions for cohesive zone models, Journal of the Mechanics and Physics of Solids 50 (4) (2002) 809–825. doi:10.1016/S0022-5096(01)00095-3.
[34] T. Diehl, On using a penalty-based cohesive-zone finite element approach, Part I: Elastic solution benchmarks, International Journal of Adhesion and Adhesives 28 (4-5) (2008) 237–255. doi:10.1016/j.ijadhadh.2007.06.003.
[35] G. Mariggiò, J. Reinoso, M. Paggi, M. Corrado, Peeling of thick adhesive interfaces: The role of dynamics and geometrical nonlinearity, Mechanics Research Communications 94 (2018) 21–27. doi:10.1016/j.mechrescom.2018.08.018.
[36] L. De Lorenzis, G. Zavarise, Modeling of mixed-mode debonding in the peel test applied to superficial reinforcements, International Journal of Solids and Structures 45 (20) (2008) 5419–5436. doi:10.1016/J.IJSOLSTR.2008.05.024.
[37] P. Lenarda, A. Gizzi, M. Paggi, A modeling framework for contact, adhesion and mechano-transduction between excitable deformable cells, European Journal of Mechanics, A/Solids 72 (March) (2017) 374–392. arXiv:1707.00920, doi:10.1016/j.euromechsol.2018.06.001.
[38] H. A. F. A. Santos, V. V. Silberschmidt, Finite Element Modelling of 2D Brittle Fracture: The Phase-Field Approach, Springer International Publishing, 2015, pp. 1–21.
[39] A. A. Griffith, VI. The phenomena of rupture and flow in solids, Philosophical Transactions of the Royal Society of London. Series A, Containing Papers of a Mathematical or Physical Character 221 (582-593) (1921) 163–198. doi:10.1098/rsta.1921.0006.
[40] G. A. Francfort, J.-J. Marigo, Revisiting brittle fracture as an energy minimization problem, Journal of the Mechanics and Physics of Solids 46 (8) (1998) 1319–1342. doi:10.1016/S0022-5096(98)00034-9.
[41] B. Bourdin, G. Francfort, J.-J. Marigo, Numerical experiments in revisited brittle fracture, Journal of the Mechanics and Physics of Solids 48 (4) (2000) 797–826. doi:10.1016/S0022-5096(99)00028-9.

[42] B. Bourdin, G. A. Francfort, J.-J. Marigo, The variational approach to fracture, Journal of Elasticity 91 (1) (2008) 5–148. doi:10.1007/s10659-007-9107-3.
[43] C. Miehe, M. Hofacker, F. Welschinger, A phase field model for rate-independent crack propagation: Robust algorithmic implementation based on operator splits, Computer Methods in Applied Mechanics and Engineering 199 (45) (2010) 2765–2778. doi:https://doi.org/10.1016/j.cma.2010.04.011.
[44] S. Conti, M. Focardi, F. Iurlano, Phase field approximation of cohesive fracture models, Annales de l'Institut Henri Poincare (C) Analyse Non Lineaire 33 (4) (2016) 1033–1067. arXiv:1405.6883, doi:10.1016/j.anihpc.2015.02.001.
[45] F. Freddi, F. Iurlano, Numerical insight of a variational smeared approach to cohesive fracture, Journal of the Mechanics and Physics of Solids 98 (2017) 156 – 171. doi:https://doi.org/10.1016/j.jmps.2016.09.003.
[46] G. Li, B. Yin, L. Zhang, K. Liew, Modeling microfracture evolution in heterogeneous composites: A coupled cohesive phase-field model, Journal of the Mechanics and Physics of Solids 142 (2020) 103968. doi:https://doi.org/10.1016/j.jmps.2020.103968.
[47] S. Zhou, T. Rabczuk, X. Zhuang, Phase field modeling of quasi-static and dynamic crack propagation: Comsol implementation and case studies, Advances in Engineering Software 122 (2018) 31–49. doi:https://doi.org/10.1016/j.advengsoft.2018.03.012.
[48] P. K. Kristensen, E. Martínez-Pañeda, Phase field fracture modelling using quasi-newton methods and a new adaptive step scheme, Theoretical and Applied Fracture Mechanics 107 (2020) 102446. doi:https://doi.org/10.1016/j.tafmec.2019.102446.
[49] M. J. Borden, T. J. Hughes, C. M. Landis, A. Anvari, I. J. Lee, A phase-field formulation for fracture in ductile materials: Finite deformation balance law derivation, plastic degradation, and stress triaxiality effects, Computer Methods in Applied Mechanics and Engineering 312 (2016) 130–166. doi:10.1016/j.cma.2016.09.005.
[50] M. Ambati, T. Gerasimov, L. De Lorenzis, Phase-field modeling of ductile fracture, Computational Mechanics 55 (5) (2015) 1017–1040. doi:10.1007/s00466-015-1151-4.
[51] A. Dean, J. Reinoso, N. K. Jha, E. Mahdi, R. Rolfes, A phase field approach for ductile fracture of short fibre reinforced composites, Theoretical and Applied Fracture Mechanics 106 (2020) 102495. doi:10.1016/J.TAFMEC.2020.102495.
[52] B. Bourdin, C. J. Larsen, C. L. Richardson, A time-discrete model for dynamic fracture based on crack regularization, International Journal of Fracture 168 (2) (2011) 133–143. doi:10.1007/s10704-010-9562-x.
[53] M. J. Borden, C. V. Verhoosel, M. A. Scott, T. J. Hughes, C. M. Landis, A phase-field description of dynamic brittle fracture, Computer Methods in Applied Mechanics and Engineering 217-220 (2012) 77–95. doi:10.1016/j.cma.2012.01.008.
[54] R. J. Geelen, Y. Liu, T. Hu, M. R. Tupek, J. E. Dolbow, A phase-field formulation for dynamic cohesive fracture, Computer Methods in Applied Mechanics and Engineering 348 (2019) 680–711. arXiv:1809.09691, doi:10.1016/j.cma.2019.01.026.
[55] J.-Y. Wu, V. P. Nguyen, C. T. Nguyen, D. Sutula, S. Sinaie, S. Bordas, Phase-field modelling of fracture, Advances in Applied Mechanics 53 (2020).
[56] K. Seleš, F. Aldakheel, Z. Tonković, J. Sorić, P. Wriggers, A general phase-field model for fatigue failure in brittle and ductile solids, Computational Mechanics 67 (5) (2021) 1431–1452. doi:10.1007/s00466-021-01996-5.
[57] P. K. Kristensen, C. F. Niordson, E. Martínez-Pañeda, A phase field model for elastic-gradient-plastic solids undergoing hydrogen embrittlement, Journal of the Mechanics and Physics of Solids 143 (2020) 104093. doi:https://doi.org/10.1016/j.jmps.2020.104093.
[58] F. Aldakheel, B. Hudobivnik, A. Hussein, P. Wriggers, Phase-field modeling of brittle fracture using an efficient virtual element scheme, Computer Methods in Applied Mechanics and Engineering 341 (2018) 443–466. doi:10.1016/j.cma.2018.07.008.
[59] F. Aldakheel, B. Hudobivnik, P. Wriggers, Virtual element formulation for phase-field modeling of ductile fracture, International Journal for Multiscale Computational Engineering 17 (2) (2019) 181–200. doi:10.1615/IntJMultCompEng.2018026804.
[60] L. Yang, Y. Yang, H. Zheng, A phase field numerical manifold method for crack propagation in quasi-brittle materials, Engineering Fracture Mechanics 241 (November 2020) (2021) 107427. doi:10.1016/j.engfracmech.2020.107427.
[61] J.-Y. Wu, V. P. Nguyen, A length scale insensitive phase-field damage model for brittle fracture, Journal of the Mechanics and Physics of Solids 119 (2018) 20–42. doi:10.1016/j.jmps.2018.06.006.
[62] V. P. Nguyen, J. Y. Wu, Modeling dynamic fracture of solids with a phase-field regularized cohesive zone model, Computer Methods in Applied Mechanics and Engineering 340 (2018) 1000–1022. doi:10.1016/j.cma.2018.06.015.
[63] J.-Y. Wu, T. K. Mandal, V. P. Nguyen, A phase-field regularized cohesive zone model for hydrogen assisted cracking, Computer Methods in Applied Mechanics and Engineering 358 (2020) 112614. doi:https://doi.org/10.1016/j.cma.2019.112614.
[64] D.-C. Feng, J.-Y. Wu, Phase-field regularized cohesive zone model (czm) and size effect of concrete, Engineering Fracture Mechanics 197 (2018) 66–79. doi:https://doi.org/10.1016/j.engfracmech.2018.04.038.
[65] P. Zhang, X. Hu, X. Wang, W. Yao, An iteration scheme for phase field model for cohesive fracture and its implementation in Abaqus, Engineering Fracture Mechanics 204 (2018) 268–287. doi:10.1016/j.engfracmech.2018.10.006.
[66] C. Miehe, L. M. Schänzel, Phase field modeling of fracture in rubbery polymers. Part I: Finite elasticity coupled with brittle failure, Journal of the Mechanics and Physics of Solids 65 (1) (2014) 93–113. doi:10.1016/j.jmps.2013.06.007.
[67] T. K. Mandal, V. P. Nguyen, J. Y. Wu, A length scale insensitive anisotropic phase field fracture model for hyperelastic composites, International Journal of Mechanical Sciences 188 (April) (2020). doi:10.1016/j.ijmecsci.2020.105941.
[68] J. Russ, V. Slesarenko, S. Rudykh, H. Waisman, Rupture of 3D-printed hyperelastic composites: experiments and phase field fracture modeling, Journal of the Mechanics and Physics of Solids (2020) 103941doi:10.1016/j.jmps.2020.103941.
[69] S. Tang, G. Zhang, T. F. Guo, X. Guo, W. K. Liu, Phase field modeling of fracture in nonlinearly elastic solids via energy decomposition, Computer Methods in Applied Mechanics and Engineering 347 (2019) 477–494.

doi:10.1016/j.cma.2018.12.035.
[70] H. Chi, O. Lopez-Pamies, G. H. Paulino, A variational formulation with rigid-body constraints for finite elasticity: theory, finite element implementation, and applications, Computational Mechanics 57 (2) (2016) 325–338. doi:10.1007/s00466-015-1234-2.
[71] A. Kumar, G. A. Francfort, O. Lopez-Pamies, Fracture and healing of elastomers: A phase-transition theory and numerical implementation, Journal of the Mechanics and Physics of Solids journal homepage 112 (2018) 523–551. doi:10.1016/j.jmps.2018.01.003.
[72] B. Talamini, Y. Mao, L. Anand, Progressive damage and rupture in polymers, Journal of the Mechanics and Physics of Solids 111 (2018) 434–457. doi:10.1016/j.jmps.2017.11.013.
[73] H. Li, Z. jun Yang, B. bei Li, J. ying Wu, A phase-field regularized cohesive zone model for quasi-brittle materials with spatially varying fracture properties, Engineering Fracture Mechanics 256 (August) (2021) 107977. doi:10.1016/j.engfracmech.2021.107977.
[74] T. T. Nguyen, J. Yvonnet, Q. Z. Zhu, M. Bornert, C. Chateau, A phase-field method for computational modeling of interfacial damage interacting with crack propagation in realistic microstructures obtained by microtomography, Computer Methods in Applied Mechanics and Engineering 312 (2016) 567–595. doi:10.1016/j.cma.2015.10.007.
[75] T. T. Nguyen, D. Waldmann, T. Q. Bui, Role of interfacial transition zone in phase field modeling of fracture in layered heterogeneous structures, Journal of Computational Physics 386 (2019) 585–610. doi:10.1016/j.jcp.2019.02.022.
[76] C. V. Verhoosel, R. de Borst, A phase-field model for cohesive fracture, International Journal for Numerical Methods in Engineering 96 (1) (2013) 43–62. doi:https://doi.org/10.1002/nme.4553.
[77] J. Vignollet, S. May, R. de Borst, C. V. Verhoosel, Phase-field models for brittle and cohesive fracture, Meccanica 49 (11) (2014) 2587–2601. doi:10.1007/s11012-013-9862-0.
[78] S. May, J. Vignollet, R. De Borst, A numerical assessment of phase-field models for brittle and cohesive fracture: Γ-Convergence and stress oscillations, European Journal of Mechanics, A/Solids 52 (2015) 72–84. doi:10.1016/j.euromechsol.2015.02.002.
[79] A. C. Hansen-Dörr, P. Hennig, M. Kästner, K. Weinberg, A numerical analysis of the fracture toughness in phase-field modelling of adhesive fracture, PAMM 17 (1) (2017) 249–250. doi:10.1002/pamm.201710094.
[80] A. C. Hansen-Dörr, R. de Borst, P. Hennig, M. Kästner, Phase-field modelling of interface failure in brittle materials, Computer Methods in Applied Mechanics and Engineering 346 (2019) 25–42. doi:https://doi.org/10.1016/j.cma.2018.11.020.
[81] M. Paggi, J. Reinoso, Revisiting the problem of a crack impinging on an interface: A modeling framework for the interaction between the phase field approach for brittle fracture and the interface cohesive zone model, Computer Methods in Applied Mechanics and Engineering 321 (2017) 145–172. arXiv:1702.01102, doi:10.1016/j.cma.2017.04.004.
[82] V. Carollo, J. Reinoso, M. Paggi, Modeling complex crack paths in ceramic laminates: A novel variational framework combining the phase field method of fracture and the cohesive zone model, Journal of the European Ceramic Society 38 (8) (2018) 2994–3003. doi:10.1016/j.jeurceramsoc.2018.01.035.
[83] M. Paggi, M. Corrado, J. Reinoso, Fracture of solar-grade anisotropic polycrystalline Silicon: A combined phase field–cohesive zone model approach, Computer Methods in Applied Mechanics and Engineering 330 (2018) 123–148. doi:10.1016/j.cma.2017.10.021.
[84] V. Carollo, J. Reinoso, M. Paggi, A 3D finite strain model for intralayer and interlayer crack simulation coupling the phase field approach and cohesive zone model, Composite Structures 182 (2017) 636–651. doi:10.1016/j.compstruct.2017.08.095.
[85] T. Guillén-Hernández, I. G. García, J. Reinoso, M. Paggi, A micromechanical analysis of inter-fiber failure in long reinforced composites based on the phase field approach of fracture combined with the cohesive zone model, International Journal of Fracture 220 (2) (2019) 181–203. doi:10.1007/s10704-019-00384-8.
[86] A. Quintanas-Corominas, A. Turon, J. Reinoso, E. Casoni, M. Paggi, J. Mayugo, A phase field approach enhanced with a cohesive zone model for modeling delamination induced by matrix cracking, Computer Methods in Applied Mechanics and Engineering 358 (2020) 112618. doi:10.1016/j.cma.2019.112618.
[87] V. Carollo, T. Guillén-Hernández, J. Reinoso, M. Paggi, Recent advancements on the phase field approach to brittle fracture for heterogeneous materials and structures, Advanced Modeling and Simulation in Engineering Sciences 5 (1) (2018) 8. doi:10.1186/s40323-018-0102-y.
[88] T. Guillén-Hernández, J. Reinoso, M. Paggi, Fracture analysis of thin films on compliant substrates: A numerical study using the phase field approach of fracture, International Journal of Pressure Vessels and Piping 175 (May) (2019) 103913. doi:10.1016/j.ijpvp.2019.05.008.
[89] V. Tvergaard, Fibre debonding and breakage in a whisker-reinforced metal, Materials Science and Engineering A 190 (1-2) (1995) 215–222. doi:10.1016/0921-5093(95)80005-0.
[90] H. D. Espinosa, P. D. Zavattieri, A grain level model for the study of failure initiation and evolution in polycrystalline brittle materials. Part I: Theory and numerical implementation, Mechanics of Materials 35 (3-6) (2003) 333–364. doi:10.1016/S0167-6636(02)00285-5.
[91] H. Amor, J.-J. Marigo, C. Maurini, Regularized formulation of the variational brittle fracture with unilateral contact: Numerical experiments, Journal of the Mechanics and Physics of Solids 57 (8) (2009) 1209–1229. doi:10.1016/j.jmps.2009.04.011.
[92] E. Tanné, T. Li, B. Bourdin, J.-J. Marigo, C. Maurini, Crack nucleation in variational phase-field models of brittle fracture, Journal of the Mechanics and Physics of Solids 110 (2018) 80–99. doi:10.1016/j.jmps.2017.09.006.
[93] A. Kumar, O. Lopez-Pamies, The phase-field approach to self-healable fracture of elastomers: A model accounting for fracture nucleation at large, with application to a class of conspicuous experiments, Theoretical and Applied Fracture Mechanics 107 (6 2020). doi:10.1016/j.tafmec.2020.102550.
[94] T. Belytschko, W. Liu, B. Moran, K. Elkhodary, Nonlinear Finite Elements for Continua and Structures, Wiley, 2013.

[95] J. Reinoso, M. Paggi, R. Rolfes, A computational framework for the interplay between delamination and wrinkling in functionally graded thermal barrier coatings, Computational Materials Science 116 (2016) 82–95. doi:10.1016/j.commatsci.2015.08.031.
[96] G. Molnár, A. Gravouil, 2D and 3D Abaqus implementation of a robust staggered phase-field solution for modeling brittle fracture, Finite Elements in Analysis and Design 130 (2017) 27–38. doi:10.1016/j.finel.2017.03.002.
[97] O. C. Zienkiewicz, R. L. Taylor, D. Fox, The Finite Element Method for Solid and Structural Mechanics: Seventh Edition, Elsevier Ltd, 2013. doi:10.1016/C2009-0-26332-X.
[98] J. Reinoso, M. Paggi, A consistent interface element formulation for geometrical and material nonlinearities, Computational Mechanics 54 (6) (2014) 1569–1581. doi:10.1007/s00466-014-1077-2.
[99] A. Vegt, van der, L. Govaert, Polymeren : van keten tot kunststof, 5th Edition, DUP Blue Print, 2003.
[100] M. Corrado, M. Paggi, J. Reinoso, Dynamic formulation of phase field fracture in heterogeneous media with finite thickness cohesive interfaces, Computational Materials Science (2021). doi:in press.
[101] F. Avilés, L. Llanes, A. I. Oliva, Elasto-plastic properties of gold thin films deposited onto polymeric substrates, Journal of Materials Science 44 (10) (2009) 2590–2598. doi:10.1007/s10853-009-3339-5.
[102] X. Meng, Z. Wang, S. Vinnikova, S. Wang, Mechanics of periodic film cracking in bilayer structures under stretching, Journal of Applied Mechanics, Transactions ASME 85 (7) (2018). doi:10.1115/1.4039757.
[103] D. Roylance, Introduction to Fracture Mechanics, 2001.
[104] L. Freund, S. Suresh, Thin Film Materials: Stress, Defect Formation and Surface Evolution, Cambridge University Press, 2004.
[105] N. Lu, J. Yoon, Z. Suo, Delamination of stiff islands patterned on stretchable substrates, Zeitschrift fuer Metallkunde/Materials Research and Advanced Techniques 98 (8) (2007) 717–722. doi:10.3139/146.101529.
[106] J. Reinoso, M. Paggi, P. Areias, A finite element framework for the interplay between delamination and buckling of rubber-like bi-material systems and stretchable electronics, Journal of the European Ceramic Society 36 (9) (2016) 2371–2382. doi:10.1016/j.jeurceramsoc.2016.01.002.

Appendix A. Benchmark tests for the phase-field approach

Appendix A.1. 2D formulation: penny shaped model

In order to demonstrate the capability of our formulation, a first benchmark test has been performed to compare to results available in [66] for the same problem. A penny-shaped specimen with a pre-existing notch in the center has been considered, with geometry and boundary conditions depicted in Fig. A.43. The test consists of a rectangular plate of 0.4mm height and 2mm width with a central horizontal notch of 0.2mm width and 0.01mm height. A monotonically increasing displacement u has been applied on the upper boundary while the bottom boundary is fixed.

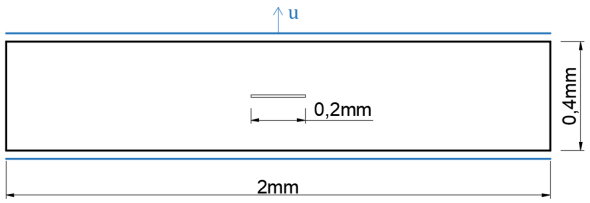

Fig. A.43: Geometry and boundary conditions of a rectangular plate with a central notch under remote displacement u.

The finite element discretization of the plate consists of around 64700 elements (characteristic element length $h = 0.002\,\text{mm}$ as in [66]). A magnification of the mesh in the area close to the central notch is shown in Fig. A.44.

Following the benchmark test proposed in [66], the plate has shear modulus $\mu = 5\text{N/mm}^2$ and Poisson ratio $\nu = 0.45$ which corresponds to $\beta = 9$. The critical fracture energy is $G_c^b = 2.4\text{N/mm}$ and the length scale is $l_0 = 0.01\,\text{mm}$, while the residual parameter k has been set to 1.0×10^{-6} (the same value is used in all the simulations of this work).

Different simulations have been performed comparing the result of the 2D plane stress and plane strain assumptions with the solution in [66]. The crack path at different imposed displacements until the complete rupture for the plane strain configuration is shown for the deformed pattern in Fig. A.45.

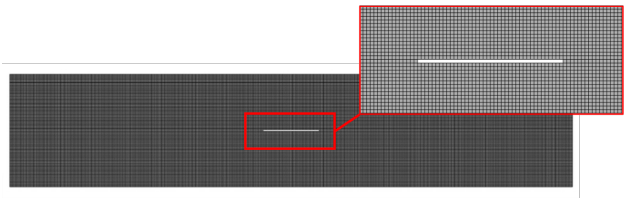

Fig. A.44: Mesh of the rectangular plate with the central notch.

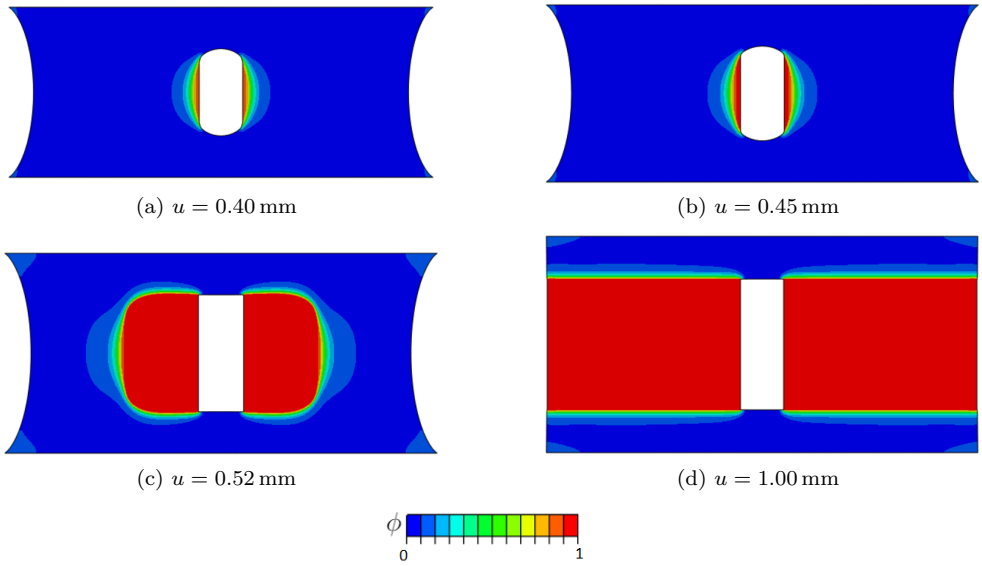

Fig. A.45: Phase-field evolution during the crack propagation for the rectangular plate under plane strain assumption.

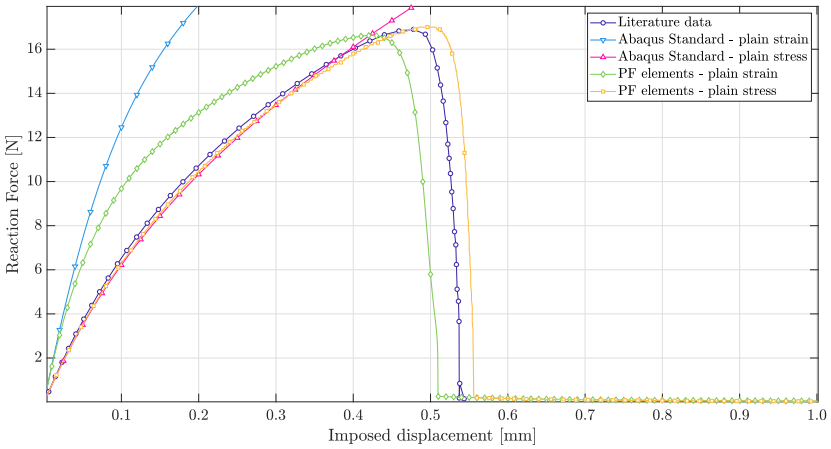

Fig. A.46: Central notched plate response in terms of reaction force-imposed displacement considering plane strain and plane stress hypotheses. Comparison between the present approach and the results obtained in [66] and using standard Abaqus hyperelastic elements.

The corresponding load-displacement curves are plotted in Fig. A.46. In these series of graphs, results with label `Abaqus` correspond to the same geometry solved with standard finite elements available in Abaqus

using the same material parameters for the Neo-Hookean model. They have been juxtaposed to the phase-field elements results in order to observe that they overlap perfectly when the plate is still undamaged, as expected. The results are in line with the benchmark test taken from [66], verifying the formulation.

Appendix A.2. 3D formulation: thin cylindrical structure

The coded phase-field element with hyperelastic material model has been used to simulate the crack initiation and propagation in a thin cylinder with a central notch. For saving computational time, only half of a cylinder has been modeled and solved considering symmetrical boundary conditions at the vertical faces and equal applied displacement at the top and bottom face. Dimensions of the cylinder are: height equal to 60 mm, internal radius equal to 52.5 mm and thickness 5 mm, as shown in Fig. A.47. The layer has a central notch with dimensions 10 mm × 1 mm.

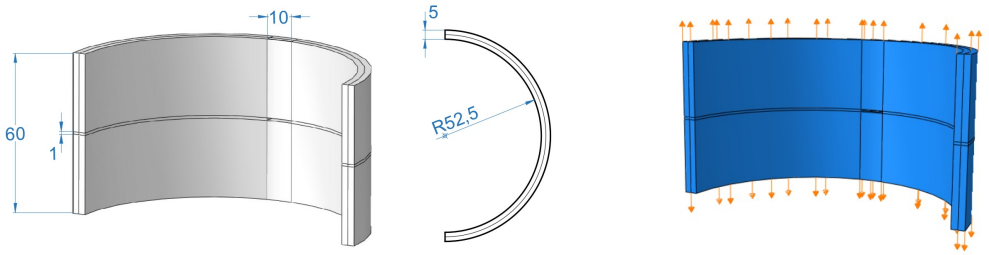

(a) (b)

Fig. A.47: Geometry (a) and boundary conditions (b) for the cylindrical layer. The dimensions are reported in mm.

The material taken into account for the simulation is the polymer PET, whose mechanical properties are shown in Tab. 1. The mesh uses 3D elements with $h = 1$ mm (see Fig. A.48) and it has been chosen in order to provide accurate results within a reasonable computational time for the simulation.

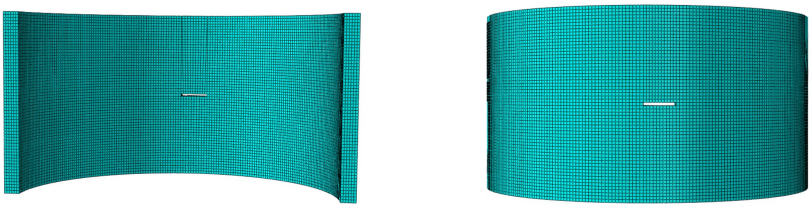

(a) (b)

Fig. A.48: Mesh of the cylinder.

The structure response in terms of reaction force-imposed displacement and the crack path are shown in Fig. A.49.

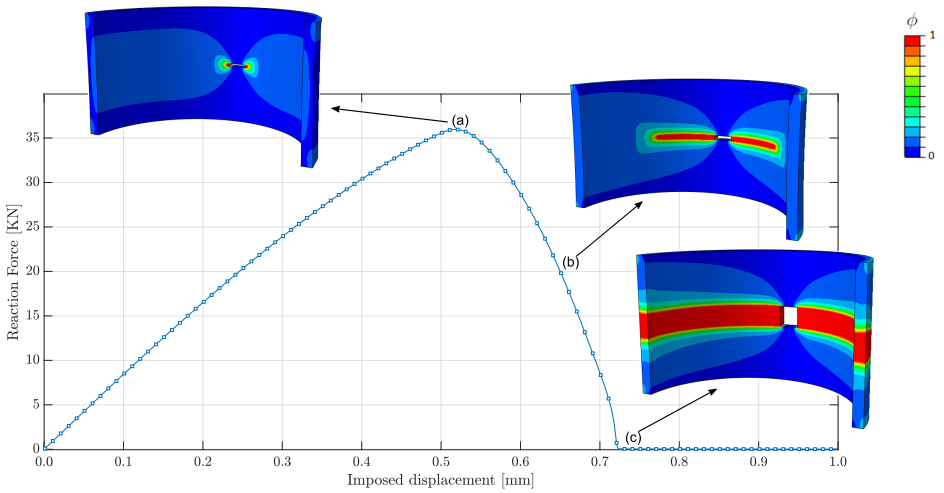

Fig. A.49: Load-displacement curve for the simulation of the cylindrical polymeric layer and snapshots of the crack path evolution.